Journal of Materials Chemistry B

ROYAL SOCIETY OF CHEMISTRY

PAPER

View Article Online
View Journal | View Issue

Check for updates

Cite this: J. Mater. Chem. B, 2025, 13, 7072

Bioinspired silk protein modification to develop instant dissolvable microneedles with superior mechanical properties and long-term biomolecule stabilization†

Jayakumar Rajendran, [a] Jeyashree K., [a] Sujith M. S., [a] Lalitha Devi Alluri[b] and Jyotsnendu Giri *[a]

Received 23rd December 2024,
Accepted 22nd April 2025

DOI: 10.1039/d4tb02836h

rsc.li/materials-b

Dissolvable microneedles (DMNs) obtained from silk proteins have been considered most promising due to the biocompatibility, tuneable mechanical properties, and superior biomolecule stabilization properties of their silk matrix, required for cold chain-free storage and transport of therapeutic biomolecules and vaccines. However, despite their excellent potential, silk-based microneedles with instant dissolvability, superior mechanical properties, and storage stability have not yet been reported. Reported DMNs prepared with <5% silk concentration without β-sheets show poor mechanical and storage stability. Conversely, silk MNs prepared using <5% silk treated with an organic solvent or >5% silk may have sufficient mechanical properties but lose their instant dissolubility due to β-sheet formation during solvent treatment and storage, respectively. Thus, herein, we address these challenges for the first time *via* the biomimetic modification of silk proteins to mimic the molecular structure of human serum albumin (HSA) and silk protein molecules in the silk gland lumen of silkworms, resulting in high solubility and low viscosity. Our biomimetic modified silk (MS) allowed us to prepare DMNs in higher concentrations (>10% w/v up to 20% w/v) with a stabilizing agent (>10% w/v), exhibiting superior mechanical properties of >45 N and instant dissolvability even after 6 months of storage at RT without inducing β-sheet formation. Furthermore, MS-DMN facilitated the exceptional storage stability of platelet-rich plasma (PRP) with >80% retention for six months when stored at 4 °C or 25 °C and >90% at 40 °C at 75% RH for one month, as confirmed through *in vitro* cell proliferation assay, in ova (CAM assay), and *in vivo* diabetic wound studies. Thus, our novel biomimetic MS-DMN exhibits superior mechanical properties and exceptional biomolecule storage stability, enabling potential cold chain-free preservation and transportation for various biomedical applications.

1. Introduction

Microneedle (MN) patches offer a novel approach for minimally invasive self-administration transdermal drug delivery by efficiently penetrating the skin layers with hundreds of micrometer-scale needles.[1–3] Based on the matrix materials used for their preparation, MNs are classified into solid, coated, hollow, dissolvable, and hydrogel microneedles. Among them, DMNs have been considered a promising system for the stable and precise intradermal delivery of biomolecules (proteins, nucleic acids, and therapeutic molecules) for various biomedical applications such as vaccines.[4–7] They offer unique advantages for delivering protein/nucleic acid therapeutics or vaccines, including (1) improving patience compliance by painless injections, (2) the possibility of enabling cold chain-free delivery and storage, and (3) eliminating the need for trained personnel for vaccination, making them suitable for mass vaccination in resource-limited settings.[8–11] However, the ideal dissolvable microneedles must possess a fracture force of at least 0.19 N per needle to penetrate the external barrier of the skin (stratum corneum) with long-term stabilization, rapid dissolution, and delivery of the encapsulated biomolecules.[12,13]

Silk proteins (fibroins from the cocoons of *Bombyx mori* silkworm) have been considered an excellent matrix material for the preparation of microneedles owing to their biocompatibility, tuneable mechanical properties, and superior biomolecule stabilization properties during storage-related stress.[14,15]

[a] Department of Biomedical Engineering, Indian Institute of Technology Hyderabad, Kandi, Telangana, 502284, India. E-mail: enarm@bme.iith.ac.in, jgiri@bme.iith.ac.in
[b] Department of Pharmacology, G. Pulla Reddy College of Pharmacy, Hyderabad, Telangana, 500028, India

† Electronic supplementary information (ESI) available. See DOI: https://doi.org/10.1039/d4tb02836h

However, despite their excellent potential, silk-based microneedles with instant dissolvability (DMN), superior mechanical properties, and storage stability have not been reported to date.[16,17] Silk proteins can change from soluble to insoluble secondary structures (β-sheets) when subjected to organic solvent treatment, high temperature, and storage, with high mechanical properties but at the expense of their instant dissolvability.[17–19] Microneedles prepared from <10% (w/v) unmodified silk solution showed inherently poor mechanical properties (<0.019 N per needle),[20,21] while approaches such as organic solvent treatment and vapor annealing resulted in improved mechanical properties with the formation of β-sheets but they lost their instant dissolvability.[22,23] Furthermore, a higher concentration of silk protein in the matrix tends to undergo self-assembly/conformational change into β-sheets during storage from less than 24 h to over 30 days but its instant dissolvability is lost.[24] Hence, this limits the use of unmodified silk to prepare instant dissolvable microneedles that can be stored for a long period at room temperature. Accordingly, stabilizing agents such as trehalose, sucrose, maltose, and mono-, di-, or polysaccharides are often used at concentrations of more than ≥5% w/v to protect and enhance the storage stability of proteins/nucleic acid biomolecules (encapsulated in MN matrix) from denaturation during drying and storage.[25,26] However, the incorporation of stabilizing agents (>5% w/v) into microneedles further decreases their fracture force to less than 0.019 N per needle, making it difficult to overcome the compressive force required to penetrate the skin.

There is an unmet need to fabricate silk-based instant dissolvable microneedles (DMNs) with superior mechanical properties and excellent storage stability (at 4 °C and 25 °C). The conventional method for the fabrication of silk DMNs using >5% w/v concentration of silk or inducing the formation of β-sheets to achieve suitable mechanical properties results in poor dissolvability. Inspired by the molecular structure of negatively charged human serum albumin (HSA)[27] and the molecular structure of silk protein in the gland lumen (MSG) (high concentration >20% w/v of silk stored without changing into insoluble β-sheets from the random coil structure).[28] Thus, herein, we address these challenges for the first time by introducing a carboxylic group in silk fibroin protein molecules to limit their intramolecular and intermolecular interaction, conformational change, and β-sheet formation at higher concentrations to improve the solubility of the silk fibroin. This biomimetic approach of carboxylic group enrichment in the modified silk (MS) results in higher solubility of >10% to 25% w/v by limiting its coil to β-sheet conversion. Moreover, it allowed the preparation of silk DMNs with higher concentrations of MS (>10% w/v to 20% w/v) and stabilizing agents (>5% w/v) but with superior mechanical properties (>0.4 N) and stabilization of biomolecules in their matrix. Even the instant dissolvability of MS-DMN remained unaffected during long-term storage at different temperatures. Novel biomimetic-modified silk protein DMNs were prepared using varying silk concentrations and evaluated for their mechanical properties, instant dissolvability, and storage stability of encapsulated model biomolecules such as platelet-rich plasma (PRP) and horse radish peroxidase (HRP). Our silk DMNs enabled more than 70% biomolecule activity to be retained after six months of storage at 4 °C/25 °C for six months and 90% activity when stored at 40 °C and 75% RH (relative humidity) for one month, which was evaluated using *in vitro* cell and in ova (CAM) assays. MS-DMN was further assessed for effective PRP transdermal delivery and PRP bioactivity retention *in vivo* using diabetic wound healing models in rats.

2. Materials and methods

2.1. Materials

Cocoons of *Bombyx mori* silkworm were obtained from the Central Silk Board in Hyderabad, India. Succinic anhydride (SA) and Rose Bengal were obtained from Sigma Aldrich, USA. Silver sulfadiazine, ex. horseradish peroxidase RZ >3.0, 250 U mg^{-1}, and *o*-phenylenediamine dihydrochloride (OPD) were obtained from Sisco Research Laboratories Pvt. Ltd (SRL), India. Analytical grade reagents and solvents were used in all experiments. PDMS microneedle molds with a needle tip width of 60 μm, needle width of 300 μm, and height of 600 μm were purchased from Micropoint Technologies Pvt Ltd, Singapore.

2.2. Modification of silk fibroin and preparation of microneedles

2.2.1. Preparation of regenerated silk fibroin (RSF) solution. The silk cocoon was cut into small pieces, followed by degumming and dissolution of the degummed cocoon. Then 0.2 M sodium carbonate solution was heated at 100 °C, and the small cocoon pieces were immediately added to the solution and treated for 30 min. The degumming was repeated twice, and then the samples were washed in DI water and dried in an oven at 60 °C overnight. The degummed fibers were dissolved in the 9.3 M LiBr solution and stirred for 2 h at 60 °C. After complete dissolution, the solution was dialyzed in a cellulose membrane (cutoff 12 400 kDa) against DI water for 3 days by changing the water every six hours. After dialysis, the solution was centrifuged at 9500 rpm for 30 min, and the regenerated silk fibroin solution was stored at 4 °C for further use. The protein concentration was measured by drying a known weight of the solution and weighing the remaining weight to yield the 4.5% w/v silk fibroin.

2.2.2. Carboxylic acid modification of RSF. The pH of 30 mL of 4.5% w/v of the RSF solution was increased to 11 using freshly prepared 0.1 M NaOH. Different concentrations of succinic anhydride (SA) (R = 5 and R = 10, where R represents the concentration in millimoles of SA) was slowly added to 1 g of RSF solution, followed by constant stirring for 2 h. After the reaction was completed, the modified silk (MS) solution was dialyzed against DI water (dialysis tube, 12 400 MWCO) for three days (water was changed every 12 h) to remove unreacted SA. The modified silk (MS) was purified by centrifuging at 9000 rpm for 20 min, freeze-dried for three days to get white fluffy MS, and stored at 4 °C for further experiments.

2.2.3. Preparation of silk microneedles. The modified silk microneedles (MS-DMN) were prepared in three different MS

concentrations (w/v) of 10% (MS10-DMN), 15% (MS15-DMN), and 20% (MS20-DMN). Similarly, for comparison, unmodified silk (UMS) microneedles (UMS-DMN) were prepared in 4.5% w/v of UMS to yield UMS4.5-DMN, which was stored for 90 days at 25 °C to get UMS4.5-DMN-RT90. UMS-DMN and MS-DMN were prepared with slight modifications to the published protocol.[29] In brief, MS and stabilizing agents (trehalose and sucrose) were dissolved in 7.4 pH PBS in varying concentrations of 7.5%, 5%, and 2.5% w/v to get MS-T7.5-DMN, MS-T5-DMN, and MS-T2.5-DMN, respectively. The respective microneedle tip solution was poured into a 10 × 10 array PDMS mold. Then, the tip solution in the mold was subjected to a positive pressure of 1 bar to fill the needle void of the mold. The positive pressure was slowly removed for 10 min, and this step was repeated three times to remove all the air bubbles from the solution. The solution in the PDMS mold was dried in a vacuum oven at 25 °C for 24 h, followed by air drying at RT (25 °C) for 24 h. The dried MS-DMNs, MS-T-DMNs, UMS-DMNs, and UMS-T-DMNs were removed from the mold, sealed in plastic bags, and stored in a desiccator under vacuum at different storage temperatures (4 °C and 25 °C) for further studies.

2.2.4. Preparation of silk microneedles loaded with different model biomolecules and drugs. To check the processing and storage stress of the biomolecules in the DMNs, model biomolecules (PRP and HRP) were loaded in UMS-DMN and MS-DMN with varying concentrations of stabilizing agent, sealed in plastic bags and stored in a desiccator under vacuum at different temperatures (4 °C and 25 °C). 1 μg of HRP was loaded in MS-DMN with varying stabilizing agent concentrations of 7.5%, 5%, and 2.5% w/v to prepare (HRP-MS-T7.5-DMN, HRP-MS-T5-DMN and HRP-MS-T2.5-DMN) and HRP-loaded UMS-DMN (HRP-UMS-T7.5-DMN, HRP-UMS-T75-DMN and HRP-UMS-T2.5-DMN), respectively.

Cord blood was provided by collaborators from Archana Hospital (Hyderabad, India). PRP was extracted from the cord blood by gradient centrifugation for 15 min at 300 g and pelted from the supernatant by centrifuging at 1000 g for 5 min at 25 °C with the approval from the Institutional Ethics Committee (approval number IITH/IEC/2018/12/13) of the Indian Institute of Technology, Hyderabad.[30] Activated PRP (freeze–thaw three times at −80 °C for 15 min and 37 °C for 5 min, then centrifuged at 9000 rpm, and the supernatant collected) was loaded in the silk microneedles (MS-DMN and UMS-DMN) with varying concentrations of stabilizing agents (5% w/v and 10% w/v of trehalose or sucrose), sealed in plastic bags and stored in a desiccator under vacuum and different storage conditions, *i.e.*, 4 °C and 25 °C. PRP-MS-DMN was prepared by loading the activated PRP in a mixture of MS-stabilizing agents at the ratio of 1 : 100 w/w and designated as PRP-MS-DMN-0 (as prepared), PRP-MS-T5-DMN-1 (1 month), PRP-MS-T5-DMN-2 (2 months), PRP-MS-T5-DMN-3 (3 months) and PRP-MS-T5-DMN-6 (6 months). The model antibacterial drug SSD was loaded in the UMS and MS-DMN to evaluate the instant dissolvability of MS-DMN and the antibacterial efficiency of the released SSD from the MS-DMNs. SSD was loaded at three different concentrations (0.5%, 1%, 2% w/v) following the above-mentioned process to get MS-DMN (SSD0.5-MS-DMN, SSD1-MS-DMN, and SSD2-MS-DMN) and UMS-DMN (SSD0.5-UMS-DMN, SSD1-UMS-DMN, and SSD2-UMS-DMN), respectively. The detailed information of the different microneedles is mentioned in the ESI,† Table S1.

2.3. Characterization of MS and UMS DMNs

2.3.1. Fourier transform infrared spectroscopy (FTIR) analysis. The chemical signature of MS and UMS, their secondary structure in the different microneedles, and their interaction with the stabilizing excipients (trehalose and sucrose) were determined using FTIR.[31,32] The varying amount of carboxylic acid modification of RSF and the dried MS-DMNs and MS-T/S-DMNs was recorded using attenuated total reflectance (ATR) FTIR (Alpha Bruker, Germany) with 128 scans for each measurement in the range of 4000–400 cm^{-1} with a resolution of 4 cm^{-1}. The secondary structure of UMS and MS was analyzed by deconvoluting the amide I region (1590–1705 cm^{-1}) of the respective FTIR spectra using OriginPro 9.0.[33] The amide I spectra were analyzed by deconvoluting them using the frequencies identified through secondary derivative analysis, and then fitted to a Lorentzian line shape. Three samples for each microneedle sample were tested (n = 3).

2.3.2. Nuclear magnetic resonance (NMR). NMR spectroscopy was performed on the UMS and MS (R = 5 and R = 10) samples to probe their chemical signature and extend of carboxylic group modification. Protein modification was confirmed using ^{1}H NMR spectroscopy on a Bruker Advance III-400 MHz spectrophotometer in deuterated water (D_2O) using tetramethylsilane (TMS) as the standard. 10 mg of each sample was weighed and dissolved in 1 mL of D_2O and analyzed for NMR characterization after complete dissolution. The degree of modification was calculated based on the integral area of the lysine residue of the RSF modified in MS (R = 5 and R = 10).

2.3.3. Determination of carboxyl content in UMS and MS. The carboxyl content in MS (R = 5 and R = 10) and UMS was determined by plotting a curve of pH *vs.* NaOH consumed using the electrical conductivity method.[34] In brief, 1.5% w/v of UMS and MS (R = 5 and R = 10) was prepared in 60 mL of DI water with constant stirring for 1 h at 37 °C. The pH of the solution was adjusted to 3.0 using 0.05 M HCl, and 0.1 M NaOH was added to the above-mentioned solution at the fixed rate of 100 μL min^{-1}. The pH was recorded after every addition up to 12 pH, and the pH *vs.* amount of NaOH consumed was plotted to calculate the carboxyl content in UMS and MS.

2.3.4. Scanning electron microscopy (SEM) analysis. The morphology of UMS-DMNs and MS-DMNs was observed using a JOEL-JSM-7600F-FESEM (JOEL, Tokyo, Japan) field emission scanning electron microscope. After preparing different silk microneedles, DMNs were sputter-coated with gold for 60 s and accelerating voltage of 3 kV for SEM analysis with a tilt of 30°.

2.3.5. Sodium dodecyl-sulfate-polyacrylamide gel electrophoresis (SDS-PAGE). According to a previously reported protocol, the extent of carboxylic group modification of silk and its molecular charges were determined using sodium dodecyl-sulfate-polyacrylamide gel electrophoresis (SDS–PAGE).[35] In brief, 0.6 mg mL^{-1} of UMS and MS solution was prepared and mixed with 5× Laemmli buffer in a 3 : 1 ratio. The solution was heated at 90 °C for 10 min, and 20 μL of the respective

solution was loaded into the 10% polyacrylamide stacking gel and 8% resolving gel. Then, the gel was run at 70 V for 60 min, stained with Coomassie R-250 (Sigma Aldrich) for 15 min, and destained with the destaining solution of 50% w/v methanol, 10% w/v acetic acid solution overnight. Finally, the gel was imaged using a ChemiDoc system (BioRad Laboratories, USA).

2.3.6. Circular dichroism (CD) spectroscopy. The protein conformation in UMS-DMN and the influence of the carboxylic modification on the protein conformation in MS-DMN and MS-T-DMN were analyzed using a JASCO J-1500 circular dichroism spectrometer with a slight modification of published protocol.[36] Briefly, 0.2 mg mL^{-1} of all variants of UMS-DMNs and MS-DMN (immediately prepared and stored for 6 months) were prepared in DI water. The respective solution was analyzed with a 1 mm path length cuvette at the scan speed of 50 nm per min from 180 to 250 nm. All measurements were performed three times, and the baseline was corrected with DI water. The spectra were processed with the JASCO spectra analyzer and plotted with OriginPro 9.

2.3.7. Instant dissolvability property. The effect of carboxylic modification on the instant dissolvability of MS-DMN was checked by inserting all the prepared variants of MS-DMN into the 20% w/v gelatin gel (mimics the hydration level of the stratum corneum).[37] UMS4.5-DMN and UMS4.5-DMN-RT90 were used to confirm the influence of the carboxylic modification on the instant dissolvability of MS-DMN even after storage for 3 months. In brief, UMS-DMN and MS-DMN were inserted into gelatin gel with a layer of parafilm to let their tip alone dissolve, and the post-dissolved DMNs were analyzed using JOEL-JSM- 7600F-FESEM (JOEL, Tokyo, Japan). The time taken to dissolve in the gelatin gel entirely was recorded and photographed using a Canon Powershot SX420 IS digital camera.

2.3.8. *Ex vivo* drug permeation study. The instant dissolvability and release of the encapsulated SSD from SSD-MS-DMN and SSD-UMS-DMNs were studied using a Franz-diffusion cell. SSD1-MS-DMN was compared with SSD1-UMS4.5-DMN and SSD1-UMS4.5-DMN-RT90. In brief, the respective SSD-loaded DMNs were inserted on the epidermis side of shaved porcine skin for 5 min to dissolve completely. The DMNs were inserted into the skin and placed on the Franz-diffusion cell, with the epidermis facing upwards. The receptor chamber was filled with 20 mL of 1 × PBS 7.4 pH, and 1 mL of PBS was added to the skin in the donor compartment to keep the skin hydrated. Then, 1 mL of PBS from the receptor chamber was collected at a predetermined interval and replaced with fresh PBS of the same volume. The collected release samples were analyzed using the SSD method developed in HPLC (Agilent Technologies 1260 Infinity II) following our previously published procedure.[38]

2.3.9. Mechanical properties and insertion capability of DMNs. The mechanical properties and insertion capability of the developed MS-DMN with varying concentrations of MS and stabilizing agents (trehalose and sucrose) were determined using a texture analyzer (TA-XT plus, Stable microsystem) and a slightly modified published protocol.[39] MS-DMNs were placed on a stainless steel flat surface with the needle oriented upwards and compressed at 0.25 mm s^{-1} by a 10 mm cylindrical probe. The pre- and post-test speeds were 1.0 mm s^{-1} with the trigger force of 0.049 N. All the microneedles were analyzed three times.

Additionally, the insertion capability of MS-DMN was assessed by loading Rose Bengal into MS20-T5-DMN. The Rose Bengal-loaded MS20-T5-DMNs were inserted onto porcine ear skin for 5 min to dissolve completely. Subsequently, the dye-imprinted area on the porcine skin was examined using an optical microscope for dye pattern analysis. To investigate the morphology of UMS-DMNs and MS-DMNs after insertion, UMS-DMNs and MS-DMNs were subjected to a 40 N probe, and the morphology of the resulting MNs was examined using SEM. The depth of MS-DMN insertion into porcine skin was assessed using an optical coherence tomography microscope (OCT Thorlabs Hyperion).[40]

2.4. Antibacterial activity of SSD-loaded silk microneedles

To determine the antibacterial efficacy of the model antibacterial drug SSD released from the MS-DMN, an antibacterial assay was performed against *Escherichia coli* (*E. coli*) and *Staphylococcus aureus* (*S. aureus*). The aim was to validate the antibacterial activity of the SSD released from SSD0.5/1/2-MS20-T5-DMNs compared with MS20-DMN and MS20-T5-DMNs serving as controls, following a modified protocol.[41] Briefly, 10^4 CFU per mL of bacterial suspension was grown at 37 °C for 24 h, and 100 μL of the bacterial suspension was plated on agar plates for colony formation, followed by imaging. MS20-DMN, MS20-T5-DMN, SSD0.5-MS20-T5-DMN, SSD1-MS20-T5-DMN, and SSD2-MS20-T5-DMN were placed on the bacterial agar plate, with the needle inserted into the plate. Subsequently, the zones of inhibition of the treated samples were observed on the *S. aureus* and *E. coli*-coated agar plates after further culture at 37 °C for 24 h. Finally, the inhibition zone diameters were captured using a Canon PowershotSX420 IS digital camera before being analyzed using the Image J software.

Also, MS20-DMN, MS20-T5-DMN, SSD0.5-MS20-T5-DMN, SSD1-MS20-T5-DMN, and SSD2-MS20-T5-DMN were incubated with the bacterial suspension at 37 °C for 24 h. Afterward, the bacterial solution was diluted by a factor of 1000, applied to an agar plate, and grown for 24 h at 37 °C. The resulting colonies on the plate after incubation were photographed using a Canon Powershot SX420 IS digital camera before being analyzed using the Image J software.

2.5. *In vitro* studies

2.5.1. Hemocompatibility. The blood compatibility of the different MS-DMNs was assessed through a hemolysis assay. In short, 500 μL of freshly drawn mouse blood was mixed with 5 mL of PBS, and then centrifuged at 10 000 rpm for five minutes. After discarding the supernatant, the process was repeated three times using 10 mL of PBS to clear the supernatant, and the cell pellet was resuspended in PBS. For the negative control, 200 μL of erythrocyte suspension with 800 μL of reverse osmosis water and 200 μL of erythrocyte suspension mixed with 800 μL of PBS was used as the positive control. MS20-DMN, MS20-T5-DMN, SSD-MS20-T5-DMN, PRP-MS20-T5-DMN, and SSD-PRP-MS20-T5-DMN were dissolved in 1 mL of PBS, after which they were added to the erythrocyte suspension

and further diluted with PBS before being incubated at 37 °C for 2 h, followed by centrifugation at 1000 rpm for 5 min. The absorbance was measured at 577 nm with an *iD5 MultiMode Plate Reader* from Molecular Devices USA to calculate the hemolysis rate.

$$\text{Hemolysis rate } \% = \frac{A - B}{C - B} \times 100 \quad (1)$$

where *A*, *B*, and *C* represent the absorbance of the experimental, negative, and positive control groups, respectively.

2.5.2. Cytotoxicity of silk microneedles

2.5.2.1. MTT assay. The cytotoxic effects of MS-DMN, MS-T-DMN, and SSD-MS-T-DMN were assessed using the MTT and Alamar blue assays.[36] In brief, HEK 293 cells were seeded in 96-well plates at a density of 3500 cells per well and allowed to grow overnight. After incubation, the medium was replaced with fresh medium, which was depicted as the untreated control. Different concentrations of MS-DMN, MS-T DMNs, and SSD-MS-T DMNs were dissolved in 1 mL of PBS, and 100 μL of the dissolved DMNs was added to the cells, and then incubated for 48 h at 37 °C with 5% CO_2. At a predetermined interval, the incubated samples were discarded, washed with PBS, and incubated with MTT (0.5 mg mL^{-1}) for 3 h. The formed formazan crystals were dissolved with 100 μL of DMSO before measuring the absorbance at 570 nm and 650 nm using an *iD5 MultiMode* Plate Reader (Molecular Devices, USA). Cell viability was calculated as follows:

$$\text{Viability } \% = \frac{\text{Absorbance of treated group} - \text{Absorabnce of blank}}{\text{Absorbance of untreated group} - \text{Absorabnce of blank}} \times 100 \quad (2)$$

2.5.2.2. Alamar blue assay. The cell metabolic activity rate was assessed using the Alamar blue assay. Following a 48-h incubation period, the supernatant was removed and replaced with 100 μL of a complete medium containing 10% (v/v) Alamar blue substrate (Himedia). The sample seeded cells were incubated for 3 h at 37 °C with 5% CO_2. After incubation, the supernatant was transferred to a 96-well plate, and the fluorescence value was recorded at the excitation and emission of 570 nm and 600 nm, respectively, using an *iD5 MultiMode Plate* Reader (Molecular Devices, USA).

2.5.2.3. Live dead assay. The cell viability of different MS-DMN types was examined using live/dead imaging on HEK293 cells. Following the above-mentioned procedure, the cells were seeded, cultured, and treated with the samples. Furthermore, the cells were stained with calcein AM (2 μM mL^{-1}, Himedia) and propidium iodide (10 μg mL^{-1}, Life Technologies) for 15 min. After incubation, the excess dye was removed by washing the cells three times with 1× PBS. Subsequently, images were captured using an Olympus fluorescence microscope (Olympus, IX73)

2.5.3. Cell morphology study.

The effect of different MS-DMNs on the morphology of the cells was examined using phalloidin staining on HEK293 cells. Following the above-mentioned procedure, the cells were seeded, cultured, and treated with the samples. After sample incubation, the cells were stained with phalloidin and Hoechst 33342 following our previously published protocol.[42] The stained cells were imaged using a fluorescence microscope (Olympus IX73 from Japan).

2.6. Bioactivity assessment and storage stability of encapsulated biomolecules in the DMNs

2.6.1. HRP activity.

To understand the impact of processing and long-term storage stress on the biomolecules loaded in MS-T-DMN, HRP was utilized as a model enzyme in MS-T-DMNs, sealed in plastic bags and stored in a desiccator under vacuum at varying temperatures (4 °C and 25 °C) for 6 months. Periodically, HRP-MS-T-DMNs were dissolved in 1 mL of PBS to assess the remaining HRP activity. A control group comprised of HRP suspension in PBS was maintained under identical conditions. An OPD-based assay was conducted with some adjustments based on published methods to determine the residual HRP activity within HRP-MS-T-DNMs.[43] Stock solutions of OPD (6.28 mM), H_2O_2 (6 mM), and varying concentrations of standard HRPs ranging from 1.5–0 nM were prepared using sodium phosphate buffer at pH 7.2. The samples were incubated with OPD (100 μL) and H_2O_2 (20 μL), followed by absorbance measurement at 417 nm after a 30 min incubation period using an *iD5 MultiMode Plate Reader*. The concentration of HRP incorporated in MS-DMN was determined against a standard curve, as shown in ESI† Fig. S11.

2.6.2. *In vitro* bioactivity.

The bioactivity of PRP in PRP-MS-T-DMNs (samples stored at 4 °C and 25 °C) was evaluated *via* a proliferation assay with UMSC cells. To understand the effect of the concentration of the stabilizing agents (0 to 10% w/v) in the microneedle matrix on the stabilization of biomolecules at 40 °C and 75% RH, MS-DMN was prepared with stabilizing agent concentrations ranging from 5% w/v to 10% w/v according to the above-mentioned procedure, sealed in a plastic bag, and stored in a stability chamber at 40 °C and 75% RH.

2.7. In ova CAM angiogenesis assay

The chorioallantoic membrane assay was used to assess the bioactivity of PRP loaded in MS20-T5-DMN with/without and stored at 25 °C for 6 months. For the in ovo CAM analysis, the dissolved microneedles (MS20-T5-DMN, PRP-MS20-T5-DMN-0, and PRP-MS20-T5-DMN-6) were applied to a living chicken embryo following slight modification to the established procedure.[44] The fertilized chicken eggs were washed with 20% PBS saline before incubation in a humidity chamber at 37.5 °C with 60% RH and carefully opened after three days of incubation. Throughout the experiment, daily monitoring ensured close tracking of the embryo viability and environmental conditions such as temperature and humidity. Before applying DMNs on day seven, they were sterilized by keeping them under UV light for one hour. On day 14, angiogenesis in the embryos for the control, PRP control, MS20-T5-DNM, PRP-MS20-T5-DNM-0, and PRP-MS20-T5-DNM-6 was assessed through digital images captured using a Canon PowerShot SX420 IS camera.

2.8. *In vivo* diabetic wound healing using PRP-loaded MS-DMN

Finally, the potential of our PRP-loaded MS-DMNs was evaluated as a model transdermal delivery system for diabetic wound healing with slight modification of the previously published protocol.[45] Sprague-Dawley rats were procured from the ICMR-National Animal Resource Facility for Biomedical Research with prior permission of the Institutional Animal Ethics Committee (IITH_IAEC_2023_M2_P09). To establish type I diabetes mellitus, the Sprague-Dawley rats were deprived of food overnight, and intraperitoneal injection of 120 mg kg^{-1} of alloxan monohydrate was performed in the subsequent morning. The rats were considered diabetic when their plasma glucose level was more than 16.7 mM and by excessive drinking, eating, urinating, and weight-loss symptoms, indicating hyperglycemia. The diabetic rats induced by alloxan were categorized into control, blank MS-T5-DMN, and SSD-PRP-MS-DMN-6, with each group containing three animals for statistical analysis. Before surgery, these diabetic rats received anesthesia with ketamine (100 mg kg^{-1}) and xylazine (10 mg kg^{-1}). The lower back of the rats was shaved, sterilized thoroughly with 70% ethanol, and using surgical blades, two 10-mm incisions made through the entire skin on either side of the vertebral column.[46] The next day after wound creation, the MS20-T5-DMN and SSD-PRP-MS20-DMN-6 microneedles were inserted into the wound by gentle pressure from the thumb for 10 min. Before their use on animals, proper sterilization procedures involved exposing all the microneedles to UV radiation. The sterilized DMNs were kept in the wound area the day after wound creation. The rats were adequately fed, watered, and monitored regularly by photographing their wounds using a Canon Powershot SX420 IS digital camera on day 0, 3, 7, and 14. The rats were euthanized on the final day of the experiment, and tissue samples from the wounds were collected, fixed, and embedded in paraffin for further analysis. Hematoxylin and eosin (H&E) were used to detect pathological alterations in the tissue at various phases of healing, as described before.[47]

2.9. Statistical analysis

All the reported data are shown as mean ± standard deviation (SD) and statistically evaluated using OriginPro 9 and GraphPad Prism 8. GraphPad Prism 8 was used to compare groups using one-way or two-way ANOVA followed by Tukey's multiple comparison test. The statistical differences between the groups are mentioned by asterisks in all the figures, *i.e.*, $P < 0.05$; **, $P < 0.01$; ***, $P < 0.001$; ****, $P < 0.0001$; and n.s (non-significant).

3. Results and discussion

3.1. Modification of silk fibroin

It is well known that RSF (UMS) mainly exists in the silk I state (high % random coil/α-helix and low % of β-sheets), and removing water molecules from the RSF results in the close packaging of the Gly–Ala–Gly region, leading to the formation of insoluble β-sheet crystals (high % β-sheet and low % random coil/α-helix). This limits the utilization of silk fibroin protein for fabricating instant dissolvable microneedles with high fracture force and rapid dissolution after incorporating a stabilizing agent with concentrations exceeding 5% w/v.[11,13] Thus, in this study, we addressed these problems for the first time by carboxylic group modification of silk fibroin protein molecules to limit their intermolecular and intramolecular interaction, which hindered coil-β-sheet formation by enhancing their solubility with low viscosity. The modified silk (MS) facilitates the fabrication of MS-DMN and MS-T-DMN with a stabilizing agent concentration of more than 10% w/v compared to UMS, as depicted in Fig. 1.

The extent of carboxylic modification in MS was confirmed by NMR, as depicted in Fig. 1B, by comparing UMS and varying degrees of modification of MS (R = 5 and R = 10) with the decrease in the intensity of the peaks at around 2.8–3 ppm, with lysine peak at 2.8–3 ppm employed as the standard for the amine group. Further, the intensity of the peak at 1.88 ppm reflecting C═O from carboxylic acid was found to be the lowest for UMS and gradually increased from MS (R = 5) (30%) to MS (R = 10) (52%), indicating a higher degree of carboxylic group modification in silk. The estimated carboxylic group content in UMS and MS (R = 5 and R = 10) is depicted in ESI,† Fig. S1B and C, showing that the content of carboxylic groups was 0.21, 0.58, and 1.1 mmol g^{-1} for UMS, MS (R = 5), and MS (R = 10), respectively. Succinic anhydride reacts with the amine group in alkaline pH (>10), but the pH of the reaction was kept above 11 to ensure the reaction with the hydroxyl group as well. In this modification, the reactant concentration (SA) drives the substitution reaction rate, as evidenced by the increase in the carboxylic group in silk as the reactant concentration (SA) proportionally increased following Le Chatelier's principle.

This modification restricted β-sheet growth in MS, as confirmed by the ATR FTIR spectra in Fig. 1C. The N–H vibration (3223 cm^{-1}) and COO (1030 cm^{-1}) and C═O stretching at around 1720 cm^{-1} increased as the molar ratio of succinic anhydride increased from R = 5 to R = 10 in the MS samples, indicating the successful attachment of succinic anhydride to the amine groups of silk fibroin.[48] To understand the secondary structure transition of UMS, the amide I spectrum (Fig. 1C) of UMS initially showed a low intensity of β-sheet (1632 cm^{-1}) and higher intensity of α-helix and random coils (1650 cm^{-1}), which gradually reversed when UMS was stored at RT for over 3 months (Fig. 1C (inset) and ESI,† Fig. S1D). MS showed a shift in the amide I peak to a higher wavenumber (1645 cm^{-1}), suggesting a higher content of α-helix and random coils due to the disruption in the β-sheets during the modification.[49,50] This was supported by quantitatively estimating the extent of the secondary structure present in UMS and MS (R = 5 and R = 10). Specifically, the amide I peak in the range of 1705–1595 cm^{-1} was deconvoluted to yield secondary derivate peaks at 1620 cm^{-1}, 1635 cm^{-1}, 1660 cm^{-1}, 1683 cm^{-1}, and 1692 cm^{-1}, which correspond to β sheet, random coil, triple helix, β-turn/sheets and β-turn, respectively.[51] The deconvoluted peaks in the FTIR spectra (ESI,† Fig. S1E) and secondary structure analysis (Fig. 1F) showed that unmodified silk had 38% β-sheet, 24% β-turn, and less than 18% random coil. After 6 months of storage at 25 °C, the secondary structure of UMS increased to 60% β-sheet, 34% β-turn,

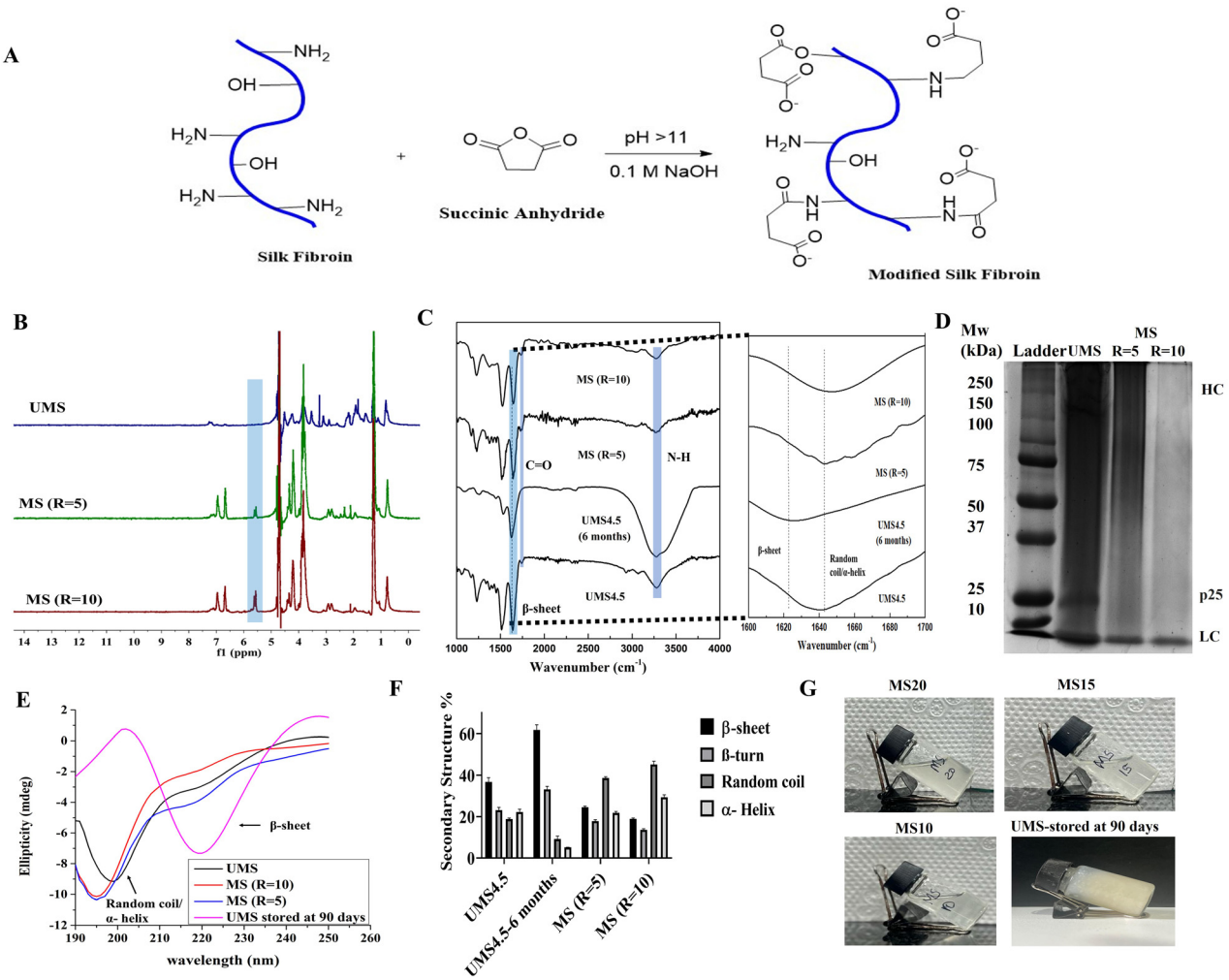

Fig. 1 (A) Chemical scheme of the modification of silk with SA. (B) NMR spectra of different MS (R = 5 and R = 10) and UMS samples, confirming the modification of silk by carboxylic groups. (C) FTIR spectra of UMS and MS (R = 5 and R = 10), showing that carboxylic group modification in silk hinders the coil-helix transition by reducing the intermolecular interaction. (D) SDS page of the UMS and MS (R = 5 and R = 10) showing less electrophoretic mobility for the MS (R = 5 and R = 10) due to the introduction of carboxylic groups, which create electrostatic repulsion with the SDS. (E) CD spectra of UMS showing a higher negative peak at 222 nm, corresponding to β-sheet, whereas MS (R = 5 and R = 10) shows a negative peak at 198 nm, corresponding to random coil/α-helix. (F) Quantitative analysis of the secondary structure calculation of MS-DMN and UMS-DMN from the deconvoluted peak of the amide I region of their FTIR spectra. (G) Solubility of various concentrations of MS10, MS15, MS20 and UMS10 when stored at RT for 90 days, resulting in gelation due to a coil-β-sheet transition, but a similar concentration of MS20 remained liquid.

and less than 10% random coil. In contrast, MS had a higher random coil content of 50%, which improved its solubility at higher concentrations and restricted the intermolecular interactions, resulting in a β-sheet content of 20%.

When the molecular weight distribution and the polarity of UMS and MS were analyzed by SDS-PAGE (Fig. 1D), UMS (lane II) showed a heavy chain (HC) of 300 kDa, a light chain (LC) of 26 kDa linked by a disulfide bond, and a P25 glycoprotein of 30 kDa, which mainly linked the HC and LC complex in the hydrophobic region.[52] In contrast, the MS samples in lanes III and IV exhibited a smeared band at around 75 and 100 kDa, which can be attributed to the introduction of succinic anhydride (SA). The modification with SA increased the net negative charges in the silk fibroin molecules, leading to altered migration patterns on the electrophoresis gel with a fixed voltage run.[35,53] The increased polarity of the silk protein due to SA modification may have also contributed to the apparent enhancement in water solubility, as depicted in Fig. 1G. Further analysis by CD, as shown in Fig. 1E, revealed that MS showed reduced intermolecular and intramolecular interaction after modification, which limited the β-sheet conversion with high steric hindrance between the carbonyl groups of MS. UMS4.5-RT90 showed a high-intensity negative peak at 222 nm and a low negative peak at 198 nm. UMS exhibited a higher content of β-sheet at 222 nm than MS (R = 5 and R = 10) and UMS4.5-RT90, which proves the carboxyl modification hindered the coil-β-sheet transition. This biomimetic modification approach helped to control the coil-β-sheet transition in the silk protein, which is beneficial for the preparation of microneedles with high mechanical strength, as discussed in the following section.

3.2. Molecular interaction between MS-stabilizing molecules

MS, in combination with stabilizing agents (trehalose, sucrose), was chosen as the matrix to fabricate MS-stabilizing agent (MS-T) complex microneedles to stabilize biomolecules. The MS-T matrix has possible intermolecular hydrogen bonding, which was studied using ATR Fourier transform infrared (FTIR) spectroscopy, and the results are shown in Fig. 2C and ESI,† Fig. S2A. In particular, MS-T-DMNs showed the C=O stretching vibrations of the amides (1650 cm^{-1}), where the N–H stretching vibration (1560 cm^{-1}) shifted to higher frequencies, and OH stretching and vibration at 3300 and 3650 cm^{-1} related to inter-hydrogen bonding of the hydroxyl group and the carboxyl group of MS, respectively.[37] The final MS-T-DMN materials lacked free hydroxyl stretching peaks, leaving only a single band in the range of 3300 cm^{-1}.[54] Upon incorporating stabilizing agents, the amide I region peak (1600–1700 cm^{-1}) showed a higher β-sheet peak of 1625 cm^{-1} for UMS4.5-DMN and UMS4.5-DMN-RT90 but was completely absent in both MS20-DMN and MS20-T5-DMN with the presence of a random coil peak (1645 cm^{-1}). Further, this peak was deconvoluted (ESI,† Fig. S2B), and the quantitative analysis (Fig. 2D) showed that the content of β-sheets decreased to less than 18% by increasing the trehalose concentration to 5% in MS20-DMN. However, there was an apparent difference in the random coil content in the MS-DMNs from 50% to 60% in MS20-DMN and MS20-T5-DMNs, respectively.

CD spectra were used to confirm the effect of modification and stabilizing agent incorporation in inhibiting the coil-β-sheet transition in MS during the fabrication of the DMNs, as shown in Fig. 2A and B, respectively. The peak intensity at 222 nm for UMS4.5-DMN and UMS4.5-DMN-RT90 was higher than that for MS-DMN, which proves that the carboxyl modification and stabilizing agent hindered the coil-β-sheet transition. MS-T-DMNs showed a lower negative peak intensity at 222 nm (β-sheet) and a higher negative peak intensity at 198 nm (random coil) than MS-DMNs, indicating that the incorporation of stabilizing agents further inhibited the coil-β-sheet transition. Alternatively, the random coil content in MS-T-DMN and MS-DMN showed a higher negative peak intensity at 198 nm than UMS4.5-DMN-RT90. This result is consistent with the FTIR data, suggesting that carboxylic group modification of the free amino and hydroxyl groups in UMS can reduce the inter- or intra-chain hydrogen bonding by inhibiting β-sheet formation, potentially aiding the storage of MS-DMN at RT.[35,36,53]

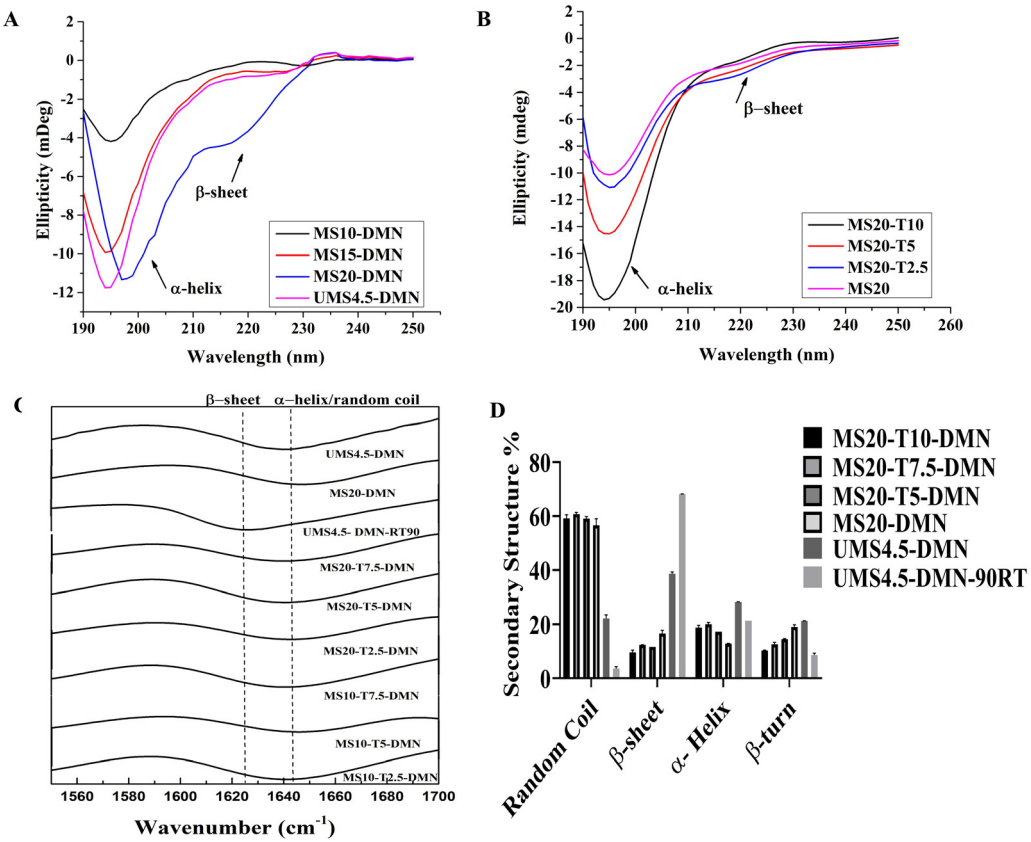

Fig. 2 (A) CD spectra of MS20-DMN, MS15-DMN, MS10-DMN, and UMS4.5-DMN. MS-DMN has a higher negative peak at 198 nm, corresponding to random coil/α-helix, while UMS4.5-DMN shows a higher negative peak at 222 nm, corresponding to β-sheet. (B) CD spectra of MS20-DMN incorporating varying stabilizing agent concentrations (5%, 7.5%, 10% w/v), showing a higher negative peak at 198 nm and suggesting the presence of a random coil/α-helix. (C) FTIR spectra of MS and MS with varying concentrations of stabilizing agents (trehalose 7.5%, 5%, and 2.5% w/v). (D) Quantitative analysis of the secondary structure determination by the deconvolution of FTIR spectra.

3.3. Physical morphologies, disintegration, and *in vitro* release of MS-DMNs

Fig. 3A shows that all the MS20-DMN, MS15-DMN, MS10-DMN, and UMS4.5-DMN tips easily dissolved when they came in contact with the interstitial fluid due to the presence of a high random coil content of more than 40%. In contrast, UMS4.5-DMN-RT90 remained insoluble and remained intact for a long time due to its higher content of β-sheet (50%) and β-turn (more than 30%), due to the coil-β-sheet transition, which was confirmed by its FTIR and CD spectra. Meanwhile, the small molecule trehalose could serve as a solubility enhancer and plasticizer, enhancing the voids within the protein-stabilizing agent complex and facilitating higher water uptake into the matrix and a higher disintegration rate.[37] Further, the dissolvability of MS-DMN and UMS-DMN was analyzed using SEM, as shown in Fig. 3C. The results revealed that MS20-DMN, MS15-DMN, MS10-DMN, and UMS4.5-DMN exhibited rapid dissolvability, whereas UMS4.5-DMN-RT90 did not dissolve when inserted in the 20% gelatin gel.

Further, MS-DMN and MS-T-DMN were stored at RT, and the effect of the storage temperature on the coil-β-sheet transition in MS-DMN was evaluated by CD spectroscopy, as depicted in ESI,† Fig. S3. In the case of UMS4.5-DMN, when stored at RT for 90 days, it showed that UMS changed in the secondary structure from random coil/α-helix to β-sheet with the intensity at 222 nm (corresponds to β-sheet) more than −5, whereas the random coil intensity at 198 was less than −2. In contrast, MS20-DMN-RT90, MS15-DMN-RT90, MS10-DMN-RT90, MS20-T5-DMN-RT90, and MS10-T5-DMN-RT90 showed a lower β-sheet intensity of less than −2, whereas the random coil and α-helix intensity at 198 nm was higher than −10. Generally, UMS has a high content of random coil/alpha helix due to the plasticization effect of water. However, removing the water from the UMS results in the close packing of the hydrophobic

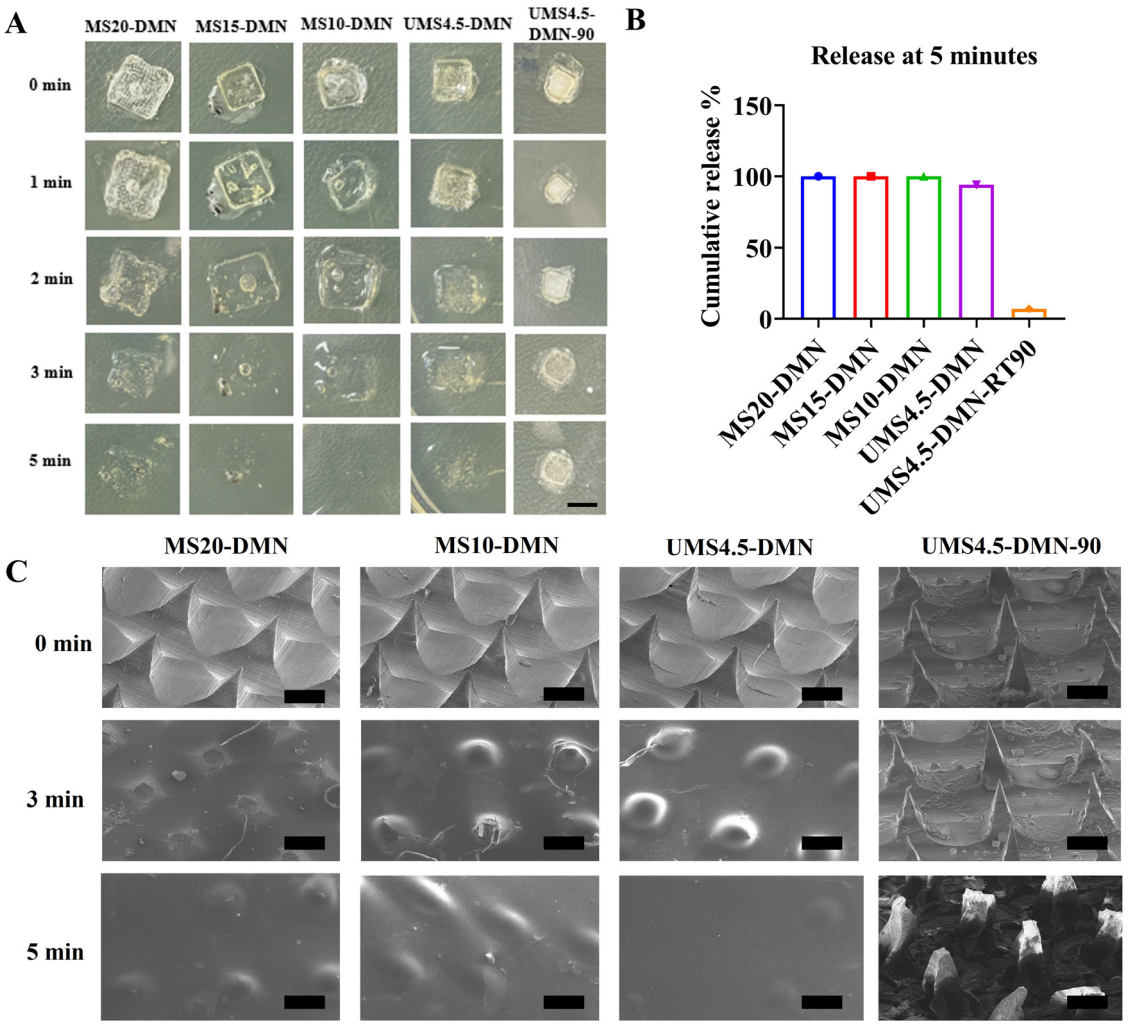

Fig. 3 (A) Representative optical images of the dissolving nature of MS20-DMN, MS15-DMN, and MS10-DMN compared with UMS4.5-DMN and UMS4.5-DMN-RT90. Scale bar: 5 mm. (B) Release profile analysis of SSD from MS-DMN and UMS-DMN, showing the immediate release of SSD from MS-DMN, whereas the UMS-DMN formulation stored for 3 months demonstrated a slower release of SSD. (C) SEM images of the dissolving nature of MS20-DMN and MS10-DMN compared with UMS4.5-DMN and UMS4.5-DMN-RT90. Scale bar: 100 μm.

region (Gly–Ala–Gly) to form β-sheets. In contrast to UMS4.5-DMN-RT90, the net negative charge of the carboxylic modification and the plasticization effect of the stabilizing agent in MS-T-DMN-RT90 helped in keeping the protein conformation, even after storage for a long time at RT. The morphology of the stored DMN was analyzed by SEM, as shown in ESI† Fig. S4, where MS-DMN retained an intact morphology and dissolvability under 5 min, even after storage at 25 °C for 6 months, except the UMS-DMN, which became brittle and prone to breakage.

The *ex vivo* skin permeation of the drug from SSD-MS-DMN was studied and compared with UMS-DMN. The total amount of drug loaded in MS-DMN was ≈454 μg for each patch, and that for UMS4.5-DMN was ≈441 μg. As shown in Fig. 3B, the cumulative release of SSD from different ratios of MS-DMN and UMS4.5-DMN was more than 100% within 5 min post-application. In contrast, that from UMS4.5-DMN-RT90 was less than 15% within 5 min, respectively, indicating that the secondary structure of UMS4.5-DMN-RT90 changes from random coil to β-sheet, resulting in gelation, which caused slow drug release from UMS4.5-DMN-RT90 (Fig. 3C).

3.4. Mechanical properties of DMNs

The mechanical robustness of microneedles is essential for their successful penetration into the skin.[55] If the needle fails to penetrate and instead interacts with the interstitial fluid, its tip may not dissolve adequately to release the intended payload. Consequently, the axial fracture force of the needle is a critical design parameter, which should exceed the resistance of the skin to ensure the integrity of the microneedle.[56,57] The moisture in DMNs can weaken their mechanical properties and reduce their instant dissolution by changing their protein conformation, ultimately resulting in poor skin penetration. The total water content in all the UMS-DMN, MS-DMN, and MS-T-DMN arrays was in the range of ∼10–12%, as shown in ESI,† Fig. S5. The mechanical strength of the microneedle arrays (MS-DMN and UMS-DMN), with and without stabilizing agents, was evaluated using a texture analyzer. MS20-DMN showed the highest fracture force of 90 N for the theoretical force required for penetration, with an average force of 0.9 N per needle. The fracture force of UMS4.5-DMN was found to be 15 N per patch, and it was even reduced after the incorporation of varying concentrations of trehalose, as shown in ESI,† Fig. S6A. Scanning electron microscopy (SEM) imaging of the needles after insertion into agarose gel using thumb pressure revealed that the MS20-DMN tips could withstand the applied force (Fig. 4C). Meanwhile, UMS4.5-DMN exhibited complete bending, as shown in Fig. 4C, indicating that MS-DMN could effectively penetrate the skin and deliver the payload. However, a lower protein concentration or higher stabilizing agent concentration

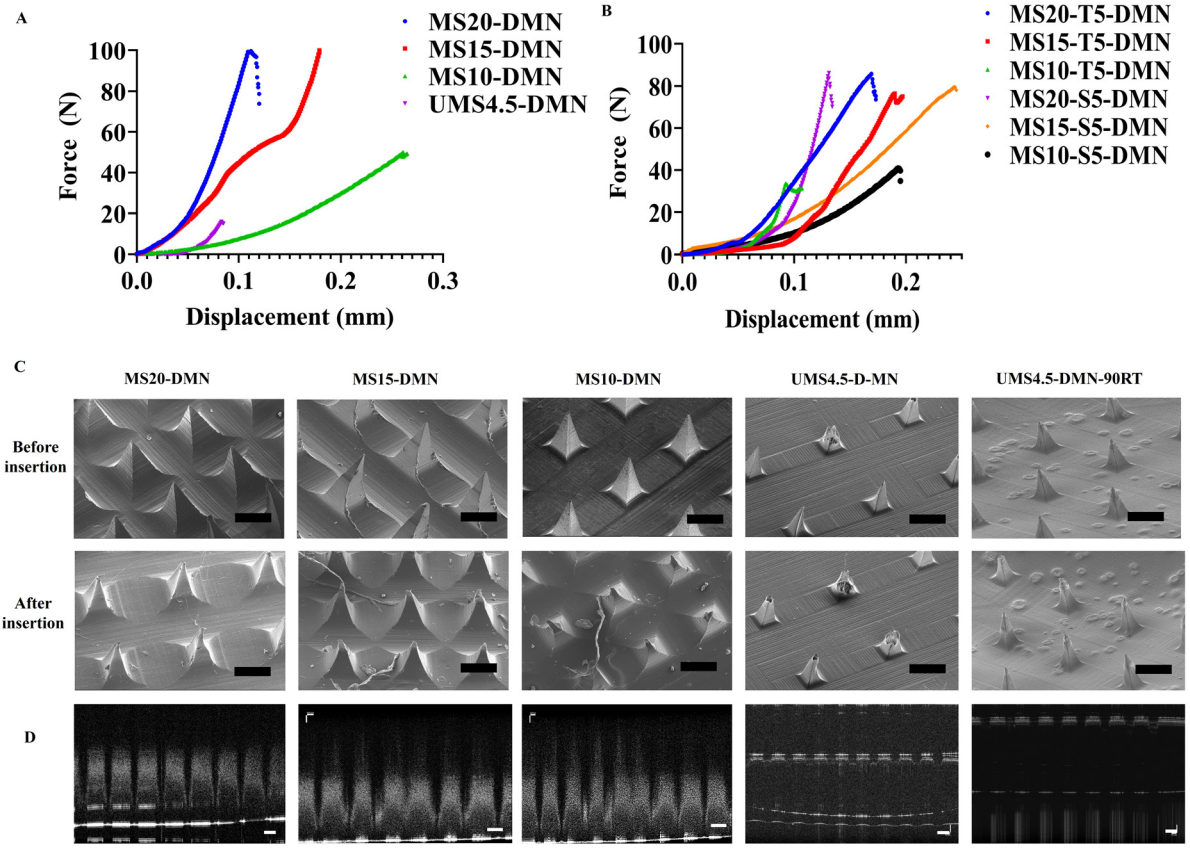

Fig. 4 Mechanical properties of the microneedles (A) prepared from various concentrations of UMS and MS-DMN. (B) Trehalose (5% w/v) incorporated in various concentrations of UMS and MS. (C) SEM images of UMS and MS-DMN before and post-insertion in 20% w/v gelatin gel. Scale bar: 200 μm. (D) After insertion on the porcine skin, OCT images with UMS and MS-DMNs were analyzed with an OCT microscope. Scale bar: 100 μm.

in the microneedle matrix resulted in a decreasing pattern in fracture force, as shown in Fig. 4b.

Given that a higher concentration of trehalose is necessary for stabilizing biomolecules, we analyzed the percentage of trehalose that can be incorporated into MS20-DMN without causing a change in the sufficient fracture force to penetrate the skin. We found that even after increasing the concentration of trehalose 5–10% w/v in PRP-SSD-MS20-DMN, the fracture force decreased from 82 N to 48 N per patch, and increasing its concentration further than 10% w/v resulted in difficulties in demolding the microneedles after their fabrication and handling (ESI,† Fig. S6B). Furthermore, isolated pig skin was used to assess the penetration capability of the various fabricated MS-DMNs. MS20-DMN was inserted into the porcine skin with thumb force and immediately withdrawn to study its morphology. The insertion was compared among the different groups, such as the MS20-T5-DMN, MS15-T5-DMN, MS10-T5-DMN, and UMS4.5-T5-DMN. Fig. 4D shows that all the MS-DMN formulations containing 5% w/v trehalose demonstrated penetration depths exceeding 300 μm, whereas the UMS4.5-T5-DMN formulation had a penetration depth of only 10 μm. The Rose Bengal-loaded MS20-T5-DMN was inserted into the skin, leaving a replica of a microchannel on the skin, indicating that MS20-T5-DMN was capable of pricking and penetrating the skin, as shown in ESI,† Fig. S6C.

3.5. Antibacterial studies

Drug-loaded microneedles can effectively deliver payloads to the inner layers of the skin, resulting in higher drug efficacy.[58,59] The antibacterial activity of silver sulfadiazine (SSD) released from the instantly dissolvable SSD-MS-DMN was evaluated using agar plate diffusion tests. All the variations of SSD-loaded microneedle-hydrogel dressings showed a zone of inhibition against both *S. aureus* and *E. coli*, except the blank MS-DMN, indicating that the drug in the microneedle tips was responsible for the antibacterial activity. Image J analysis was performed to quantify the zones of inhibition. The *E. coli* cultured plates, when treated with SSD0.5-MS20-DMN, SSD1-MS20-DMN, and SSD2-MS20-DMN, showed zones of inhibition measuring 63, 78, and 83 mm, respectively (ESI,† Fig. S7A). The zones of inhibition of *S. aureus* on the agar plates treated with SSD0.5-MS20-DMN, SSD1-MS20-DMN, and SSD2-MS20-DMN measured 21.89, 34 and 48 mm, respectively. Furthermore, the SSD2-MS20-DMN sample exhibited the highest inhibition zone, suggesting it had the best SSD activity and required the lowest dose to be effective as an antibacterial agent. The antibacterial activity of SSD-MS-DMN was also evaluated using a time-kill assay, as shown in ESI† Fig. S7D, which showed that bacterial growth was suppressed to a greater extent in all the SSD0.5-MS20-DMN, SSD1-MS20-DMN, and SSD2-MS20-DMN samples compared to the control group (MS20-DMN) following co-culturing with *E. coli* and *S. aureus*. These results suggest that the SSD-MS20-DMN formulation exhibited bactericidal activity even at the lowest concentration (0.5 mg mL^{-1}), which represents an optimal antibacterial concentration to avoid any possible toxicity from SSD in both *in vitro* and *in vivo* settings while analyzing the bioactivity of PRP.

3.6. Biocompatibility and biosafety of MS-DMNs

The biocompatibility of various silk DMN patches loaded with stabilizing agents is shown in Fig. 5. The MTT assay revealed that MS20-DMN, MS15-DMN, and MS10-DMN exhibited cell viability exceeding 80%. The incorporation of stabilizing agents and SSD into MS-DMNs did not significantly impact the cell viability, maintaining over 70% across the different DMN formulations. However, an increase in the trehalose concentration in the DMNs resulted in severe cytotoxicity, further inhibiting the proliferation of HEK293 cells. Consequently, a 5% w/v trehalose concentration was selected as the final matrix for the preparation of DMNs, given that it exhibited a favorable toxicity profile and desirable mechanical properties for insertion. The fluorescence imaging of HEK293 cells showed that MS20-T5-DMN, MS15-T5-DMN, and MS10-T5-DMN exhibited better cell proliferation with a higher cell density compared to MS20-DMN, which is consistent with the cell viability measurements using the MTT and Alamar assays, as shown in Fig. 5A and ESI,† Fig. S8A. Furthermore, the cell morphology after the incubation of the DMNs was evaluated using phalloidin staining (Fig. 5B), and the results indicated that the cells incubated with MS-DMN, MS-T-DMN, and SSD-MS-T-DMN had a better cell density without any observable changes in their morphology. The stained F-actin microfilaments and nuclei showed comparable cell localization and expansion to the control, suggesting that these DMNs were biocompatible and did not induce alterations in the cellular morphology.[60] Additionally, the hemolysis assay (Fig. 5D) demonstrated that all the samples, regardless of trehalose or SSD in MS-DMN, exhibited minimal red blood cell death, except that incorporating PRP caused some red blood cell clotting, resulting in cell death, which was almost negligible compared to the controls.

3.7. Storage stability of biomolecules in MS-DMNs

The stability of biomolecules is crucial for biomolecule delivery systems given that they undergo various processes and storage-related stress, reducing their therapeutic efficiency.[29] This study aimed to improve the stability of PRP/HRP as model biomolecules loaded in DMNs by mixing with the optimized MS-stabilizing agents and storing them at different temperatures, as depicted in Fig. 6. When stored at 4 °C for one month, the PRP-MS20-T5-MN group exhibited relative HRP activity of more than 80%, and 70% when stored at 25 °C for over six months (Fig. 6A). In the case of the groups without stabilizing agents, a higher concentration of MS in MS20-DMN was better than MS15-DMN, and MS10-DMN was found to retain greater activity, aligning with the hypothesis that the carboxylic groups and hydrogen bonding were responsible for the protection of HRP (Fig. 1 and 2). When the stabilizing agents were added, the HRP stabilization increased further due to the synergetic effect of the hydrogen bonding and glassy matrix formation.[61–64] We further explored the stabilization effect using another biomolecule (PRP) and observed a similar pattern of bioactivity retention as HRP (Fig. 6B and C). The bioactivity of PRP was analyzed using *in vitro* cell proliferation and CAM assays.

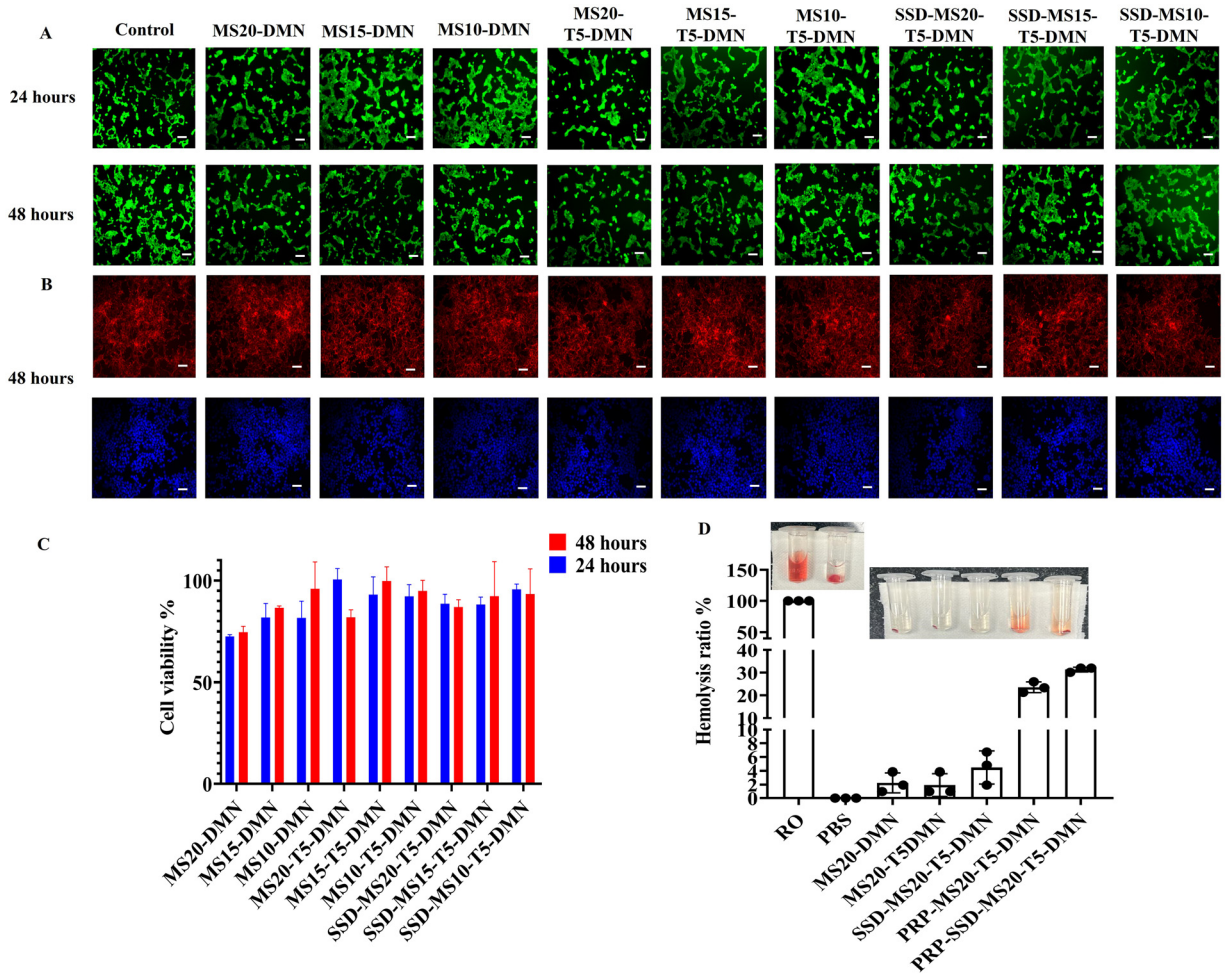

Fig. 5 (A) Live dead staining images of HEK293 cells with various microneedles for 24 and 48 h, showing more than 70% cell viability for all the MS-DMN groups. Scale bar: 100 μm. (B) Actin phalloidin staining and DAPI of HEK293 cells incubated with microneedles for 24 and 48 h, showing that all MS-DMN groups showed an intact cell morphology. Scale bar: 100 μm. (C) Quantitative analysis of biocompatibility of various microneedles incubated with HEK293 cells using MTT assay. (D) Blood compatibility behavior of the various MS-DMN performed using hemolysis assay, showing minimal red blood cell death.

To confirm the functional activity of PRP *in vitro* using the cell (UMSCs) proliferation assay, the PRP-MS-DMN samples were dissolved and PRP released from them stored for six months at 4 °C and 25 °C was quantified. The PRP released after six months of storage at 25 °C showed no significant difference between DMN without storage, with a proliferation rate of more than 95% for all the PRP-MS20-T5-DMN-(0, 1, 2, 3, 6), which was better than that of MS20-T5-DMN of 58% within 48 h (Fig. 6C). The fluorescence images of the PRP-treated UMSC showed no significant difference in fluorescence between PRP-MS20-T5-DMN with different storage conditions (0, 1, 2, 3, and 6 months) and PRP control, as depicted in Fig. 6D. The bioactivity of PRP-MS20-T5-DMN stored at 4 °C was evaluated using an *in vitro* bioactivity assay and it was found that the proliferation was more than 95% for PRP-MS20-T5-DMN kept at 0, 3, and 6 months (ESI,† Fig. S9).

Specifically, the approach to address biomolecule instability involves incorporating a higher concentration of stabilizing agent to reduce the mobility of the biomolecules during drying or dehydration.[64] However, an increase in the concentration of stabilizing agent (>5% w/v) in silk microneedles substantially reduces their mechanical properties. Here, up to 10% w/v stabilizing agent could be incorporated the microneedle-based drug delivery system (MS-DMN) without compromising its mechanical properties (ESI,† Fig. S4B). Furthermore, MS20-DMN fabricated with a trehalose concentration of 10% w/v could maintain the bioactivity of PRP-MS20-T10-DMN at more than 80% even when stored at an elevated temperature of 40 °C for 30 days. The 10% w/v trehalose (95%) better preserved the bioactivity of the platelet-rich plasma (PRP) compared to 5% w/v trehalose (85%) when stored at 40 °C and 75% relative humidity for 30 days (Fig. 7). The PRP bioactivity in the microneedles under different storage conditions was further evaluated by the CAM assay, which is discussed in the following section.

3.8. In ova angiogenesis study

The CAM assay, one of several functional assays, offers an easy-to-use and adaptable animal model to study angiogenesis and metastasis.[65] As shown in Fig. 6E, the current work used the in ovo CAM assay to assess the biological activity and storage stability of PRP in DMNs after being stored at different temperatures for six months.

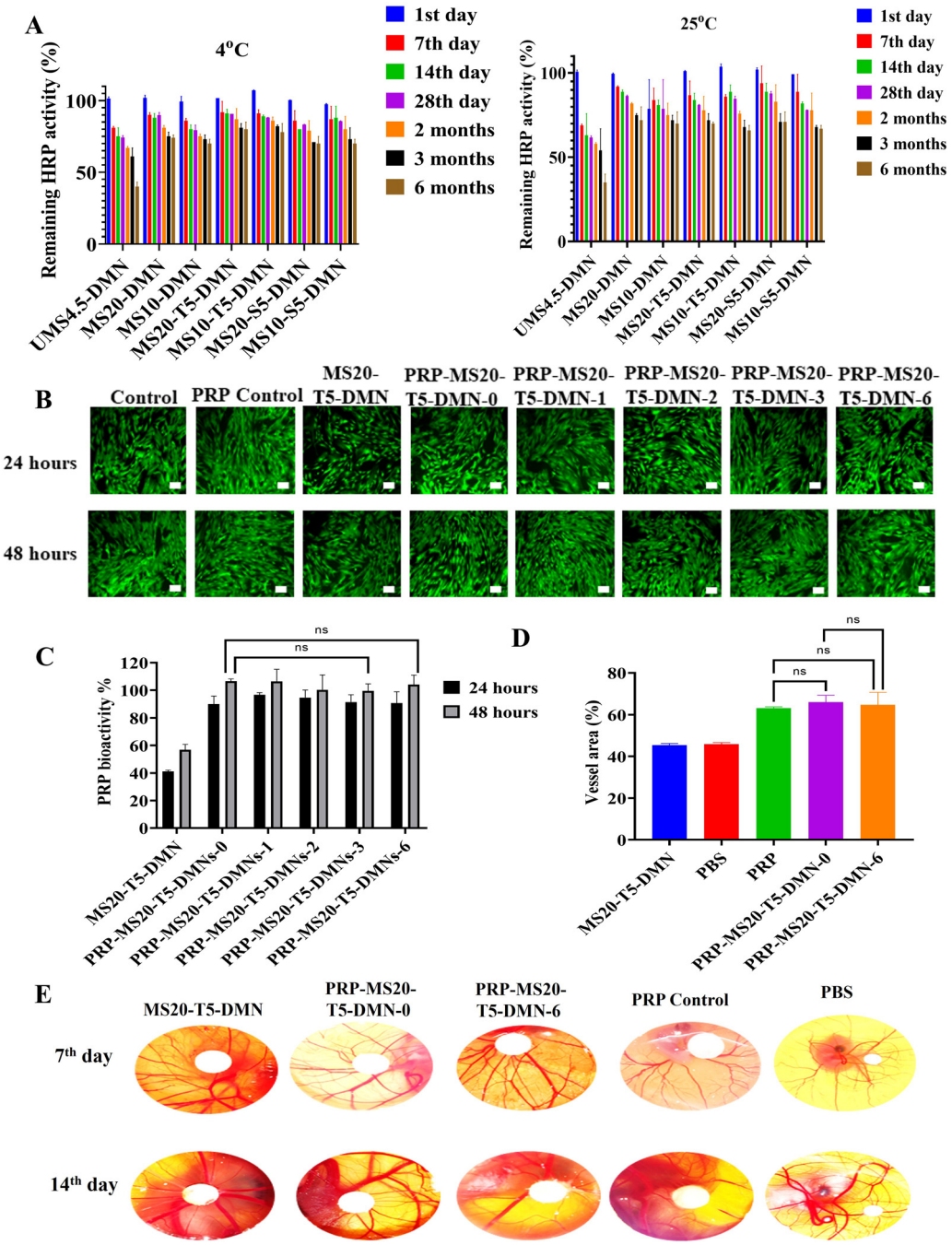

Fig. 6 Effect of processing and storage on HRP and PRP loaded in HRP/PRP-MS-DMN. (A) HRP enzymatic assay was performed to study the remaining bioactivity of the HRP loaded in HRP-MS-DMN when stored under different storage conditions of 4 °C and 25 °C for one month. (B) Live dead images of stored PRP-MS20-T5-DMN and PRP-MS20-T5-DMN (0, 1, 2, 3, 6) incubated with UMSC cells for 48 h using calcein AM and PI staining. Scale bar: 100 μm. (C) PRP bioactivity in MS-DMN and MS-T-DMN analyzed *in vitro* by incubating the stored PRP-MS20-T5-DMN and PRP-MS20-T5-DMN (0, 1, 2, 3, 6) with UMSC cells for 48 h and checked with Alamar blue assay. (D) Quantitative analysis of the percentage of vessel area in MS20-T5-DMN, PRP-MS20-DMN-(0, 1, 2, 3, 6) incubated samples in the egg through CAM assay compared with PBS and PRP control. (E) Angiogenic activity of PRP in the stored MS20-T5-DMN and MS20-T5-DMN-(0 and 6) samples checked in ova through CAM assay.

We found that PRP-MS20-T5-DMN induced blood vessel formation (53% new vessel formation) earlier than MS20-T5-DMN (40% new vessel formation) and the PRP control (45% new vessel formation) because of the potential of PRP to release a cocktail of molecules containing various growth factors, cytokines, which help in fibroblast recruitment, and collagen deposition, aiding the angiogenic process. Indeed, the blood vessel area resulting from the PRP-MS20-T5-DMN scaffolds on bay 7 was more significant than MS20-T5-DMN on the same embryonic day (Fig. 6D). This was evident when the number of

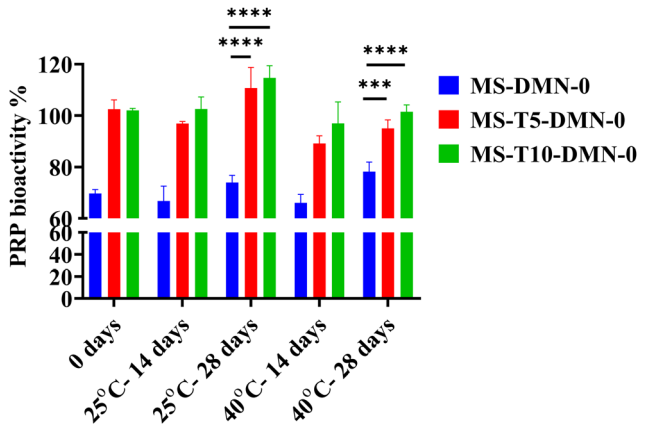

Fig. 7 Accelerated bioactivity assessment of PRP-loaded MS20-T5-DMN stored at 40 °C at 75% relative humidity compared with PRP-loaded MS20-T5-DMN stored at 25 °C for one month.

vessel junctions was analyzed; it was found that the MS20-T5-DMN group had 505 vessel junctions that were better than the control group (190). At the same time, the PRP group had better vessel junction formation without any significant difference between the PRP-MS20-T5-DMN-0 (918) and PRP-MS20-T5-DMN-6 (900) groups (Fig. 6E). The percentage of newly created arterioles was a good indicator of the PRP effect and a measure of the efficacy of PRP-MS20-T5-DMN. PRP-MS20-T5-DMN-(0, 1, 2, 3, 6) had increased angiogenic capacity compared to MS20-T5-DMN. This proves that there was no significant decrease in PRP activity in PRP-MS20-T5-DMN-6, and these findings indicate that MS20-T5-DMN can maintain the activity of PRP at 4 °C and 25 °C for six months.

The rationale is that adding trehalose reduces the mobility of the biomolecules by acting as a plasticizer and providing hydrogen bonding, thereby mitigating the denaturation of the biomolecules. Consequently, a higher trehalose concentration further helps restrict biomolecule mobility during drying. This protein-sugar matrix ensures the activity of PRP during fabrication, maintains its activity, and exhibits enhanced PRP bioactivity even after storage for six months at 25 °C and 4 °C. This improved storage stability can be leveraged to prepare clinical products, which will benefit the extended transport time of products before reaching end-users.

3.9. *In vivo* studies

The bioactivity of PRP after the processing and storage stress in SSD-PRP-MS20-T5-DMN (6 months) was evaluated using a diabetic wound healing model. Diabetic wounds were treated with SSD-PRP-MS20-T5-DMN, MS20-T5-DMN, and a control. The MS20-T5-DMN and the SSD-PRP-MS20-T5-DMN groups had blisters, which seemed more apparent on day three following treatment. Meanwhile, the control group treated with 10% saline still had a significant wound area and no visible formation of blisters even after day 7. On day seven, there was no significant decrease in wound area in all the groups. After 14 days, the control and blank DMN groups displayed comparable wound area closure rates of 73.6% and 80.8%, respectively (Fig. 8A and ESI,† Fig. S10). SSD-PRP-MS20-T5-DMN showed a complete wound closure rate of 100% in 14 days. The comparison of the wound regions treated with various samples over time indicated that MS20-T5-DMN had a minimum effect on diabetic wound healing compared to SSD-PRP-MS20-T5-DMN (Fig. 8A). Thus, combining SSD and PRP in MS-DMN, owing to their antioxidant and angiogenic properties, significantly accelerated wound healing.

A histological analysis of the wound site after the implantation of the patches was performed to determine the biocompatibility of DMNs and efficacy of PRP. Fig. 8B demonstrates that the control group showed a normal morphology of the epidermal and dermal layer of skin with moderate muscular layer inflammation and infiltration of lymphocytes and proliferation of connective tissue in the muscular layer (yellow arrow). Meanwhile, the MS20-T5-DMN group showed moderate epidermal re-epithelization (red arrow) along with dermal fibrosis, and the proliferation of fibrous tissue was observed (green arrow). In the case of the SSD-PRP-MS20-T5-DMN group, a normal epidermal morphology was seen.

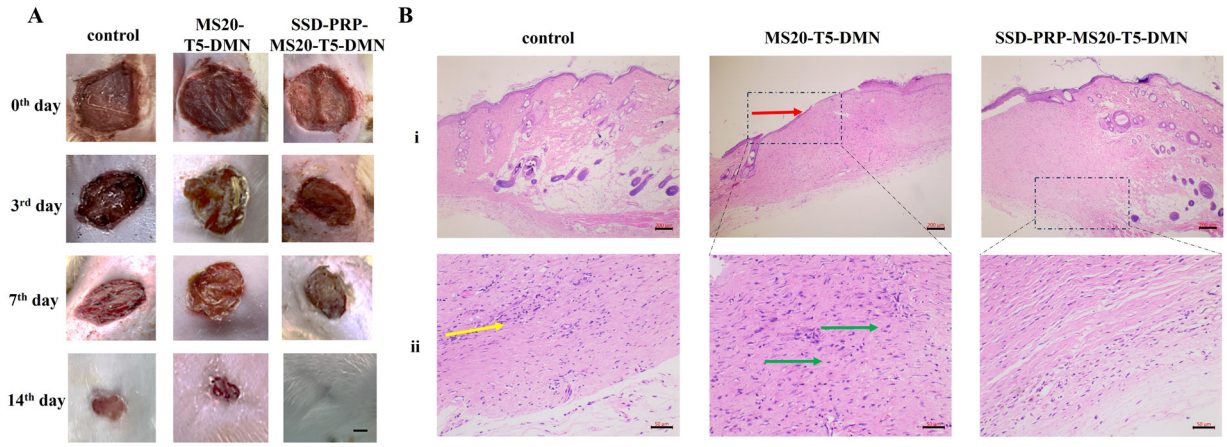

Fig. 8 (A) PRP activity in PRP-MS20-T5-DMN stored for six months at RT in a diabetic wound rat model and images of the wound closure of diabetic rats treated with the PBS control, MS20-T5-DMNs, and PRP-MS20-T5-DMNs-6. Scale bar: 2 mm. (B) H&E staining images of the wound of diabetic rats on day 14 treated with PBS control, MS20-T5-DMNs, and PRP-MS20-T5-DMNs-6. (i) 4×. Scale bar: 200 μm. (ii) 200×. Scale bar: 50 μm.

However, the dermal region and dermal layer of the skin (inset figure) showed severe proliferation of fibrous tissue/connective tissue with few foci of angiogenesis compared with other groups. As reported in the literature, the carboxylic modification of silk enhances macrophage polarization from M1 to M2, resulting in better tissue regeneration properties with low expression of pro-inflammatory cytokines.[48] On day 14, the SSD-PRP-MS20-T5-DMN group demonstrated mature granulation tissue, high angiogenic and fibroblast recruitment with visible dermis, and epidermis layer regeneration. Moreover, on day 14, the MS20-T5DMN group exhibited sufficient proliferation and angiogenic activity on the dermis layer, while the control group showed minimal inflammatory cells with less proliferation (Fig. 8B(ii)). SSD-PRP-MS20-T5-DMN showed a better therapeutic efficacy because of the unique combination of the instant release of the antioxidant SSD, the deposited ECM-like MS, and PRP, which helped in fibroblast recruitment and collagen deposition, promoting wound healing.

4. Conclusion

The conventional silk microneedles prepared using $>5\%$ w/v of silk and a stabilizing agent rely on β-sheet induction to impart high mechanical strength to pierce the stratum corneum but lose their instant solubility due to the hydrophobic nature of the β-sheets. In summary, we reported a unique biomimetic method for the modification of silk (MS), mimicking the silk protein ($>20\%$ w/v) storage in the MSG *lumen* to achieve superior solubility with restricted β-sheet growth. The prepared MS-DMN patches showed instant solubility and superior mechanical strength of >45 N, surpassing most currently available silk-based DMNs without inducing β-sheet formation. Additionally, MS-DMN could disintegrate even after long-term storage at 25 °C owing to the reduced inter/intermolecular interactions, which were difficult to control in unmodified or native silk-based DMNs. The combined effect of MS and the stabilizing agent ensured that MS20-T5-DMN retained more than 70% of PRP and HRP activity when stored at 4 °C and 25 °C for six months and more than 90% at a higher temperature (40 °C and 75% RH) for one month. The bioactivity of PRP was retained in MS-DMN and showed an effective wound healing rate *in vivo*. This biomimetic approach provides a solution for preparing silk-based DMNs with high mechanical strength without inducing β-sheet formation and a platform to stabilize biomolecules at RT. The initial assessment of MS-DMN showed that it provided better storage stability of PRP for more than six months at RT; thus, we are translating its potential in vaccine delivery application with model antigens.

Abbreviations

MN	Microneedle
DMN	Dissolvable microneedle
RSF	Regenerated silk fibroin
PRP	Platelet-rich plasma
HRP	Horse radish peroxidase
MS	Modified silk
UMS	Unmodified silk
SSD	Silver sulfadiazine
PDMS	Polydimethylsiloxane
PBS	Phosphate buffer saline
RT	Room temperature
RH	Relative humidity
T_g	Glass transition temperature
CAM	Chorioallantoic membrane assay
MTT	3-(4,5-Dimethylthiazol-2-yl)-2,5-diphenyltetrazolium bromide
HEK293	Human embryonic kidney cells
UMSC	Human umbilical mesenchymal stem cells
UV	Ultraviolet

Data availability

The data supporting this article have been included as part of the ESI.†

Conflicts of interest

The authors declare that they do not have any conflict of interest.

Acknowledgements

This work was supported by the Department of Biotechnology, Ministry of Science and Technology, India (BT/PR36505/NNT/28/1818/2022), Department of Science and Technology, Ministry of Science and Technology, India (SR/NM/-NS-1364/2014(G)), DST-Science and Engineering Research Board (SB/S3/CE/048/2015), CRG/2020/005244 and IMPRINT (DST/IMP/2018/000687), Abdul Kalam Technology Innovation National Fellowship, Indian National Academy of Engineering, India (INAE/121/AKF/37) and Ministry of education for Prime Minister Research Fellowship (PMRF) of author Jayakumar Rajendran.

References

1 J. H. Jung and S. G. Jin, Microneedle for Transdermal Drug Delivery: Current Trends and Fabrication, *J. Pharm. Invest.*, 2021, **51**(5), 503–517, DOI: 10.1007/s40005-021-00512-4.
2 J. Chen, H. Ren, P. Zhou, S. Zheng, B. Du, X. Liu and F. Xiao, Microneedle-Mediated Drug Delivery for Cutaneous Diseases, *Front. Bioeng. Biotechnol.*, 2022, **10**, 1032041, DOI: 10.3389/fbioe.2022.1032041.
3 A. Sadeqi, G. Kiaee, W. Zeng, H. Rezaei Nejad and S. Sonkusale, Hard Polymeric Porous Microneedles on Stretchable Substrate for Transdermal Drug Delivery, *Sci. Rep.*, 2022, **12**(1), 1853, DOI: 10.1038/s41598-022-05912-6.
4 B. Yavuz, L. Chambre, K. Harrington, J. Kluge, L. Valenti and D. L. Kaplan, Silk Fibroin Microneedle Patches for the Sustained Release of Levonorgestrel, *ACS Appl. Bio Mater.*, 2020, **3**(8), 5375–5382, DOI: 10.1021/acsabm.0c00671.

5 J. A. Stinson, W. K. Raja, S. Lee, H. B. Kim, I. Diwan, S. Tutunjian, B. Panilaitis, F. G. Omenetto, S. Tzipori and D. L. Kaplan, Silk Fibroin Microneedles for Transdermal Vaccine Delivery, *ACS Biomater. Sci. Eng.*, 2017, **3**(3), 360–369, DOI: **10.1021/acsbiomaterials.6b00515**.

6 Z. Wang, Z. Yang, J. Jiang, Z. Shi, Y. Mao, N. Qin and T. H. Tao, Silk Microneedle Patch Capable of On-Demand Multidrug Delivery to the Brain for Glioblastoma Treatment, *Adv. Mater.*, 2022, **34**(1), 2106606, DOI: **10.1002/adma.202106606**.

7 J. A. Stinson, A. V. Boopathy, B. M. Cieslewicz, Y. Zhang, N. W. Hartman, D. P. Miller, M. Dirckx, B. L. Hurst, E. B. Tarbet, J. A. Kluge and K. M. Kosuda, Enhancing Influenza Vaccine Immunogenicity and Efficacy through Infection Mimicry Using Silk Microneedles, *Vaccine*, 2021, **39**(38), 5410–5421, DOI: **10.1016/j.vaccine.2021.07.064**.

8 C. Z. Ng, Y. L. Lean, S. F. Yeoh, Q. Y. Lean, K. S. Lee, A. K. Suleiman, K. B. Liew, Y. W. Kassab, Y. M. Al-Worafi and L. C. Ming, Cold Chain Time- and Temperature-Controlled Transport of Vaccines: A Simulated Experimental Study, *Clin. Exp. Vaccine Res.*, 2020, **9**(1), 8, DOI: **10.7774/cevr.2020.9.1.8**.

9 S. P. Sullivan, D. G. Koutsonanos, M. Del Pilar Martin, J. W. Lee, V. Zarnitsyn, S.-O. Choi, N. Murthy, R. W. Compans, I. Skountzou and M. R. Prausnitz, Dissolving Polymer Microneedle Patches for Influenza Vaccination, *Nat. Med.*, 2010, **16**(8), 915–920, DOI: **10.1038/nm.2182**.

10 M. J. Mistilis, J. C. Joyce, E. S. Esser, I. Skountzou, R. W. Compans, A. S. Bommarius and M. R. Prausnitz, Long-Term Stability of Influenza Vaccine in a Dissolving Microneedle Patch, *Drug Delivery Transl. Res.*, 2017, **7**(2), 195–205, DOI: **10.1007/s13346-016-0282-2**.

11 W. Li, R. N. Terry, J. Tang, M. R. Feng, S. P. Schwendeman and M. R. Prausnitz, Rapidly Separable Microneedle Patch for the Sustained Release of a Contraceptive, *Nat. Biomed. Eng.*, 2019, **3**(3), 220–229, DOI: **10.1038/s41551-018-0337-4**.

12 J.-H. Park and M. R. Prausnitz, Analysis of Mechanical Failure of Polymer Microneedles by Axial Force, *J. Korean Phys. Soc.*, 2010, **56**(4), 1223–1227, DOI: **10.3938/jkps.56.1223**.

13 G. Bonfante, H. Lee, L. Bao, J. Park, N. Takama and B. Kim, Comparison of Polymers to Enhance Mechanical Properties of Microneedles for Bio-Medical Applications, *Micro Nano Syst. Lett.*, 2020, **8**(1), 13, DOI: **10.1186/s40486-020-00113-0**.

14 G. H. Altman, F. Diaz, C. Jakuba, T. Calabro, R. L. Horan, J. Chen, H. Lu, J. Richmond and D. L. Kaplan, Silk-Based Biomaterials, *Biomaterials*, 2003, **24**(3), 401–416, DOI: **10.1016/S0142-9612(02)00353-8**.

15 N. A. Guziewicz, A. J. Massetti, B. J. Perez-Ramirez and D. L. Kaplan, Mechanisms of Monoclonal Antibody Stabilization and Release from Silk Biomaterials, *Biomaterials*, 2013, **34**(31), 7766–7775, DOI: **10.1016/j.biomaterials.2013.06.039**.

16 M. Zhu, Y. Liu, F. Jiang, J. Cao, S. C. Kundu and S. Lu, Combined Silk Fibroin Microneedles for Insulin Delivery, *ACS Biomater. Sci. Eng.*, 2020, **6**(6), 3422–3429, DOI: **10.1021/acsbiomaterials.0c00273**.

17 S. Wang, M. Zhu, L. Zhao, D. Kuang, S. C. Kundu and S. Lu, Insulin-Loaded Silk Fibroin Microneedles as Sustained Release System, *ACS Biomater. Sci. Eng.*, 2019, **5**(4), 1887–1894, DOI: **10.1021/acsbiomaterials.9b00229**.

18 M. Aoki, Y. Masuda, K. Ishikawa and Y. Tamada, Fractionation of Regenerated Silk Fibroin and Characterization of the Fractions, *Molecules*, 2021, **26**(20), 6317, DOI: **10.3390/molecules26206317**.

19 I. Taketani, S. Nakayama, S. Nagare and M. Senna, The Secondary Structure Control of Silk Fibroin Thin Films by Post Treatment, *Appl. Surf. Sci.*, 2005, **244**(1–4), 623–626, DOI: **10.1016/j.apsusc.2004.09.167**.

20 Q. Zhang, L. Shi, H. He, X. Liu, Y. Huang, D. Xu, M. Yao, N. Zhang, Y. Guo, Y. Lu, H. Li, J. Zhou, J. Tan, M. Xing and G. Luo, Down-Regulating Scar Formation by Microneedles Directly *via* a Mechanical Communication Pathway, *ACS Nano*, 2022, **16**(7), 10163–10178, DOI: **10.1021/acsnano.1c11016**.

21 X. Cheng, Y. Yang, Z. Liao, Q. Yi, Y. Zhou, X. Dai, Y. Liu and O. Liu, Drug-Loaded Mucoadhesive Microneedle Patch for the Treatment of Oral Submucous Fibrosis, *Front. Bioeng. Biotechnol.*, 2023, **11**, 1251583, DOI: **10.3389/fbioe.2023.1251583**.

22 X. Lu, Y. Sun, M. Han, D. Chen, A. Wang and K. Sun, Silk Fibroin Double-Layer Microneedles for the Encapsulation and Controlled Release of Triptorelin, *Int. J. Pharm.*, 2022, **613**, 121433, DOI: **10.1016/j.ijpharm.2021.121433**.

23 Z. Yin, D. Kuang, S. Wang, Z. Zheng, V. K. Yadavalli and S. Lu, Swellable Silk Fibroin Microneedles for Transdermal Drug Delivery, *Int. J. Biol. Macromol.*, 2018, **106**, 48–56, DOI: **10.1016/j.ijbiomac.2017.07.178**.

24 U.-J. Kim, J. Park, C. Li, H.-J. Jin, R. Valluzzi and D. L. Kaplan, Structure and Properties of Silk Hydrogels, *Biomacromolecules*, 2004, **5**(3), 786–792, DOI: **10.1021/bm0345460**.

25 W. Wang, Lyophilization and Development of Solid Protein Pharmaceuticals, *Int. J. Pharm.*, 2000, **203**(1–2), 1–60, DOI: **10.1016/s0378-5173(00)00423-3**.

26 J. C. Joyce, M. L. Collins, P. A. Rota and M. R. Prausnitz, Thermostability of Measles and Rubella Vaccines in a Microneedle Patch, *Adv. Ther.*, 2021, **4**(10), 2100095, DOI: **10.1002/adtp.202100095**.

27 R. M. Kramer, V. R. Shende, N. Motl, C. N. Pace and J. M. Scholtz, Toward a Molecular Understanding of Protein Solubility: Increased Negative Surface Charge Correlates with Increased Solubility, *Biophys. J.*, 2012, **102**(8), 1907–1915, DOI: **10.1016/j.bpj.2012.01.060**.

28 X. Li, L. Wu, M. Huang, H. Shao and X. Hu, Conformational Transition and Liquid Crystalline State of Regenerated Silk Fibroin in Water, *Biopolymers*, 2008, **89**(6), 497–505, DOI: **10.1002/bip.20905**.

29 V. D. Bui, S. Son, W. Xavier, V. Q. Nguyen, J. M. Jung, J. Lee, S. Shin, W. Um, J. Y. An, C. H. Kim, Y. Song, Y. Li and J. H. Park, Dissolving Microneedles for Long-Term Storage and Transdermal Delivery of Extracellular Vesicles, *Biomaterials*, 2022, **287**, 121644, DOI: **10.1016/j.biomaterials.2022.121644**.

30 R. Mani, P. Roopmani, J. Rajendran, S. Maharana and J. Giri, Cord Blood Platelet Rich Plasma (PRP) as a Potential Alternative to Autologous PRP for Allogenic Preparation and Regenerative Applications, *Int. J. Biol. Macromol.*, 2024, **262**, 129850, DOI: **10.1016/j.ijbiomac.2024.129850**.

31 J. L. Gornall and E. M. Terentjev, Concentration-Temperature Superposition of Helix Folding Rates in Gelatin, *Phys. Rev. Lett.*, 2007, **99**(2), 028304, DOI: 10.1103/PhysRevLett.99.028304.

32 F. Polyak and G. Reich, Infrared Spectroscopic Study of the Coil-Helix Transition of Highly Concentrated Gelatin Formulations, *Eur. J. Pharm. Biopharm.*, 2019, **140**, 11–19, DOI: 10.1016/j.ejpb.2019.04.010.

33 M. Voicescu, S. Ionescu and C. L. Nistor, Spectroscopic Study of 3-Hydroxyflavone - Protein Interaction in Lipidic Bi-Layers Immobilized on Silver Nanoparticles, *Spectrochim. Acta, Part A*, 2017, **170**, 1–8, DOI: 10.1016/j.saa.2016.06.039.

34 T. Saito and A. Isogai, TEMPO-Mediated Oxidation of Native Cellulose. The Effect of Oxidation Conditions on Chemical and Crystal Structures of the Water-Insoluble Fractions, *Biomacromolecules*, 2004, **5**(5), 1983–1989, DOI: 10.1021/bm0497769.

35 M. R. Bet, G. Goissis and C. A. Lacerda, Characterization of Polyanionic Collagen Prepared by Selective Hydrolysis of Asparagine and Glutamine Carboxyamide Side Chains, *Biomacromolecules*, 2001, **2**(4), 1074–1079, DOI: 10.1021/bm0001188.

36 M. Zhu, Y. Wang, G. Ferracci, J. Zheng, N.-J. Cho and B. H. Lee, Gelatin Methacryloyl and Its Hydrogels with an Exceptional Degree of Controllability and Batch-to-Batch Consistency, *Sci. Rep.*, 2019, **9**(1), 6863, DOI: 10.1038/s41598-019-42186-x.

37 A. Hou, G. Quan, B. Yang, C. Lu, M. Chen, D. Yang, L. Wang, H. Liu, X. Pan and C. Wu, Rational Design of Rapidly Separating Dissolving Microneedles for Precise Drug Delivery by Balancing the Mechanical Performance and Disintegration Rate, *Adv. Healthcare Mater.*, 2019, **8**(21), 1900898, DOI: 10.1002/adhm.201900898.

38 R. Singh, P. Roopmani, M. Chauhan, S. M. Basu, W. Deeksha, M. D. Kazem, S. Hazra, E. Rajakumara and J. Giri, Silver Sulfadiazine Loaded Core-Shell Airbrushed Nanofibers for Burn Wound Healing Application, *Int. J. Pharm.*, 2022, **613**, 121358, DOI: 10.1016/j.ijpharm.2021.121358.

39 H. Chen, B. Wu, M. Zhang, P. Yang, B. Yang, W. Qin, Q. Wang, X. Wen, M. Chen, G. Quan, X. Pan and C. Wu, A Novel Scalable Fabrication Process for the Production of Dissolving Microneedle Arrays, *Drug Delivery Transl. Res.*, 2019, **9**(1), 240–248, DOI: 10.1007/s13346-018-00593-z.

40 R. F. Donnelly, M. J. Garland, D. I. J. Morrow, K. Migalska, T. R. R. Singh, R. Majithiya and A. D. Woolfson, Optical Coherence Tomography Is a Valuable Tool in the Study of the Effects of Microneedle Geometry on Skin Penetration Characteristics and In-Skin Dissolution, *J. Controlled Release*, 2010, **147**(3), 333–341, DOI: 10.1016/j.jconrel.2010.08.008.

41 S. Gao, W. Zhang, X. Zhai, X. Zhao, J. Wang, J. Weng, J. Li and X. Chen, An Antibacterial and Proangiogenic Double-Layer Drug-Loaded Microneedle Patch for Accelerating Diabetic Wound Healing, *Biomater. Sci.*, 2023, **11**(2), 533–541, DOI: 10.1039/D2BM01588A.

42 R. Singh, S. Khan, S. M. Basu, M. Chauhan, N. Sarviya and J. Giri, Fabrication, Characterization, and Biological Evaluation of Airbrushed Gelatin Nanofibers, *ACS Appl. Bio Mater.*, 2019, **2**(12), 5340–5348, DOI: 10.1021/acsabm.9b00636.

43 J. Bao, S. Xu, L. Zhao, G. Peng and H. Lu, Colorimetric and Fluorescent Dual-Mode Strategy for Sensitive Detection of Sulfide: Target-Induced Horseradish Peroxidase Deactivation, *Spectrochim. Acta, Part A*, 2020, **236**, 118296, DOI: 10.1016/j.saa.2020.118296.

44 L. Abune, N. Zhao, J. Lai, B. Peterson, S. Szczesny and Y. Wang, Macroporous Hydrogels for Stable Sequestration and Sustained Release of Vascular Endothelial Growth Factor and Basic Fibroblast Growth Factor Using Nucleic Acid Aptamers, *ACS Biomater. Sci. Eng.*, 2019, **5**(5), 2382–2390, DOI: 10.1021/acsbiomaterials.9b00423.

45 W. Liu, X. Zhai, X. Zhao, Y. Cai, X. Zhang, K. Xu, J. Weng, J. Li and X. Chen, Multifunctional Double-Layer and Dual Drug-Loaded Microneedle Patch Promotes Diabetic Wound Healing, *Adv. Healthcare Mater.*, 2023, **12**(23), 2300297, DOI: 10.1002/adhm.202300297.

46 Z. Qian, H. Wang, Y. Bai, Y. Wang, L. Tao, Y. Wei, Y. Fan, X. Guo and H. Liu, Improving Chronic Diabetic Wound Healing through an Injectable and Self-Healing Hydrogel with Platelet-Rich Plasma Release, *ACS Appl. Mater. Interfaces*, 2020, **12**(50), 55659–55674, DOI: 10.1021/acsami.0c17142.

47 Y. Zhang, S. Wang, Y. Yang, S. Zhao, J. You, J. Wang, J. Cai, H. Wang, J. Wang, W. Zhang, J. Yu, C. Han, Y. Zhang and Z. Gu, Scarless Wound Healing Programmed by Core-Shell Microneedles, *Nat. Commun.*, 2023, **14**(1), 3431, DOI: 10.1038/s41467-023-39129-6.

48 Z. Sun, R. Huang, H. Lyu, X. Yu, W. Wang, J. Li, X. Lu and C. Guo, Silk Acid as an Implantable Biomaterial for Tissue Regeneration, *Adv. Healthcare Mater.*, 2023, **12**(28), 2301439, DOI: 10.1002/adhm.202301439.

49 A. R. Murphy, P. John and D. L. Kaplan, Modification of Silk Fibroin Using Diazonium Coupling Chemistry and the Effects on hMSC Proliferation and Differentiation, *Biomaterials*, 2008, **29**(19), 2829–2838, DOI: 10.1016/j.biomaterials.2008.03.039.

50 O. Hasturk, K. E. Jordan, J. Choi and D. L. Kaplan, Enzymatically Crosslinked Silk and Silk-Gelatin Hydrogels with Tunable Gelation Kinetics, Mechanical Properties and Bioactivity for Cell Culture and Encapsulation, *Biomaterials*, 2020, **232**, 119720, DOI: 10.1016/j.biomaterials.2019.119720.

51 L. Dou, B. Li, K. Zhang, X. Chu and H. Hou, Physical Properties and Antioxidant Activity of Gelatin-Sodium Alginate Edible Films with Tea Polyphenols, *Int. J. Biol. Macromol.*, 2018, **118**, 1377–1383, DOI: 10.1016/j.ijbiomac.2018.06.121.

52 S. Inoue, K. Tanaka, F. Arisaka, S. Kimura, K. Ohtomo and S. Mizuno, Silk Fibroin of Bombyx Mori Is Secreted, Assembling a High Molecular Mass Elementary Unit Consisting of H-Chain, L-Chain, and P25, with a 6:6:1 Molar Ratio, *J. Biol. Chem.*, 2000, **275**(51), 40517–40528, DOI: 10.1074/jbc.M006897200.

53 Z. Zhang, W. Liu, D. Li and G. Li, Physicochemical Properties of Succinylated Calfskin Pepsin-Solubilized Collagen, *Biosci., Biotechnol., Biochem.*, 2007, **71**(8), 2057–2060, DOI: 10.1271/bbb.70055.

54 S. Kubo and J. F. Kadla, Hydrogen Bonding in Lignin: A Fourier Transform Infrared Model Compound Study, *Biomacromolecules*, 2005, **6**(5), 2815–2821, DOI: **10.1021/bm050288q**.

55 A. Than, C. Liu, H. Chang, P. K. Duong, C. M. G. Cheung, C. Xu, X. Wang and P. Chen, Self-Implantable Double-Layered Micro-Drug-Reservoirs for Efficient and Controlled Ocular Drug Delivery, *Nat. Commun.*, 2018, **9**(1), 4433, DOI: **10.1038/s41467-018-06981-w**.

56 M. T. C. McCrudden, A. Z. Alkilani, C. M. McCrudden, E. McAlister, H. O. McCarthy, A. D. Woolfson and R. F. Donnelly, Design and Physicochemical Characterisation of Novel Dissolving Polymeric Microneedle Arrays for Transdermal Delivery of High Dose, Low Molecular Weight Drugs, *J. Controlled Release*, 2014, **180**, 71–80, DOI: **10.1016/j.jconrel.2014.02.007**.

57 O. Olatunji, D. B. Das, M. J. Garland, L. Belaid and R. F. Donnelly, Influence of Array Interspacing on the Force Required for Successful Microneedle Skin Penetration: Theoretical and Practical Approaches, *J. Pharm. Sci.*, 2013, **102**(4), 1209–1221, DOI: **10.1002/jps.23439**.

58 S. Lyu, Z. Dong, X. Xu, H.-P. Bei, H.-Y. Yuen, C.-W. James Cheung, M.-S. Wong, Y. He and X. Zhao, Going below and beyond the Surface: Microneedle Structure, Materials, Drugs, Fabrication, and Applications for Wound Healing and Tissue Regeneration, *Bioact. Mater.*, 2023, **27**, 303–326, DOI: **10.1016/j.bioactmat.2023.04.003**.

59 T.-M. Tuan-Mahmood, M. T. C. McCrudden, B. M. Torrisi, E. McAlister, M. J. Garland, T. R. R. Singh and R. F. Donnelly, Microneedles for Intradermal and Transdermal Delivery, *Eur. J. Pharm. Sci.*, 2013, **50**(5), 623–637, DOI: **10.1016/j.ejps.2013.05.005**.

60 A. Singh, S. Kumar, C. Goswami and L. Goswami, Montmorillonite-Reinforced Xanthan Gum-Based Biomaterial Enhances Biomineralization Suitable for Bone Tissue Engineering, *Mater. Today Chem.*, 2024, **38**, 102067, DOI: **10.1016/j.mtchem.2024.102067**.

61 B. Wang, S. Tchessalov, M. T. Cicerone, N. W. Warne and M. J. Pikal, Impact of Sucrose Level on Storage Stability of Proteins in Freeze-Dried Solids: II. Correlation of Aggregation Rate with Protein Structure and Molecular mobility**This Work Is a Product of the U.S. Government and Is Not Subject to Copyright in the United States, *J. Pharm. Sci.*, 2009, **98**(9), 3145–3166, DOI: **10.1002/jps.21622**.

62 M. T. Cicerone and C. L. Soles, Fast Dynamics and Stabilization of Proteins: Binary Glasses of Trehalose and Glycerol, *Biophys. J.*, 2004, **86**(6), 3836–3845, DOI: **10.1529/biophysj.103.035519**.

63 M. T. Cicerone and J. F. Douglas, β-Relaxation Governs Protein Stability in Sugar-Glass Matrices, *Soft Matter*, 2012, **8**(10), 2983, DOI: **10.1039/c2sm06979b**.

64 M. A. Mensink, H. W. Frijlink, K. van der Voort Maarschalk and W. L. J. Hinrichs, How Sugars Protect Proteins in the Solid State and during Drying (Review): Mechanisms of Stabilization in Relation to Stress Conditions, *Eur. J. Pharm. Biopharm.*, 2017, **114**, 288–295, DOI: **10.1016/j.ejpb.2017.01.024**.

65 C. D. Stern, The Chick, *Dev. Cell*, 2005, **8**(1), 9–17, DOI: **10.1016/j.devcel.2004.11.018**.